

Mixing effects on apparent reaction rates and isotope fractionation during denitrification in a heterogeneous aquifer

Christopher T. Green,¹ John Karl Böhlke,² Barbara A. Bekins,¹ and Steven P. Phillips³

Received 16 November 2009; revised 18 March 2010; accepted 28 April 2010; published 13 August 2010.

[1] Gradients in contaminant concentrations and isotopic compositions commonly are used to derive reaction parameters for natural attenuation in aquifers. Differences between field-scale (apparent) estimated reaction rates and isotopic fractionations and local-scale (intrinsic) effects are poorly understood for complex natural systems. For a heterogeneous alluvial fan aquifer, numerical models and field observations were used to study the effects of physical heterogeneity on reaction parameter estimates. Field measurements included major ions, age tracers, stable isotopes, and dissolved gases. Parameters were estimated for the O₂ reduction rate, denitrification rate, O₂ threshold for denitrification, and stable N isotope fractionation during denitrification. For multiple geostatistical realizations of the aquifer, inverse modeling was used to establish reactive transport simulations that were consistent with field observations and served as a basis for numerical experiments to compare sample-based estimates of “apparent” parameters with “true” (intrinsic) values. For this aquifer, non-Gaussian dispersion reduced the magnitudes of apparent reaction rates and isotope fractionations to a greater extent than Gaussian mixing alone. Apparent and true rate constants and fractionation parameters can differ by an order of magnitude or more, especially for samples subject to slow transport, long travel times, or rapid reactions. The effect of mixing on apparent N isotope fractionation potentially explains differences between previous laboratory and field estimates. Similarly, predicted effects on apparent O₂ threshold values for denitrification are consistent with previous reports of higher values in aquifers than in the laboratory. These results show that hydrogeological complexity substantially influences the interpretation and prediction of reactive transport.

Citation: Green, C. T., J. K. Böhlke, B. A. Bekins, and S. P. Phillips (2010), Mixing effects on apparent reaction rates and isotope fractionation during denitrification in a heterogeneous aquifer, *Water Resour. Res.*, 46, W08525, doi:10.1029/2009WR008903.

1. Introduction

[2] Natural attenuation is a critical factor controlling the long-term fate and transport of contaminants in many aquifer settings, and proper management of these resources requires accurate characterization of the prevailing reactions [National Research Council, 2000]. This consideration is especially important for NO₃⁻, which typically originates from widespread nonpoint sources, occupies large aquifer volumes, and is difficult to remediate with engineered solutions. The problem of NO₃⁻ contamination is mitigated at many locations by denitrification, which reduces NO₃⁻ to N₂ gas. For denitrification in aquifers, many studies have estimated reaction kinetic coefficients, the O₂ inhibition threshold for denitrification, and stable isotope fractionation effects of denitrification to improve understanding and prediction of NO₃⁻ distributions [e.g., Vogel *et al.*, 1981; Mariotti *et al.*, 1988; Böttcher *et al.*, 1990; Smith *et al.*, 1991; Mengis *et al.*, 1999; Böhlke *et al.*, 2002; Groffman *et al.*, 2006; Green *et al.*, 2008a; McMahon *et al.*, 2008]. Results

are variable, however, and more work is needed to determine relationships among these different estimates and their applicability in different settings.

[3] One source of variability and uncertainty in estimates of denitrification parameters is the effect of mixing during transport. Commonly, kinetic reaction coefficients in groundwater are estimated from gradients in groundwater travel time, reactant and product concentrations, and/or stable isotope ratios that change during the course of reactions and are used to infer reaction progress (the fraction of reactant that has been eliminated by the reaction). Such estimates commonly involve the assumption of simplified transport in which all water and solute in a given sample have the same travel time and reaction history. In reality, however, a groundwater sample consists of a mixture of waters and solutes with unknown distributions of travel times, recharge compositions, and reaction histories. As a result, estimated reaction rates and isotope fractionation parameters may not correspond to actual intrinsic values; they are, instead, “apparent” values that depend on the physical processes controlling the travel time distributions.

[4] The problem of evaluating mixing of differently aged waters in a single groundwater sample has been addressed in various ways. Analytical solutions for homogeneous aquifers with simple flow conditions have been used commonly with environmental tracer data relating to groundwater

¹U.S. Geological Survey, Menlo Park, California, USA.

²U.S. Geological Survey, Reston, Virginia, USA.

³U.S. Geological Survey, Sacramento, California, USA.

age [e.g., Zuber, 1986; Cook and Böhlke, 2000]. To account for effects of dispersion, additional methods exist for estimating the mean and higher moments of distributions of travel times at a point in space [Varni and Carrera, 1998], and to solve numerically the groundwater age equation [Woolfenden and Ginn, 2009]. In general, these efforts have focused on relatively homogeneous geological domains, whereas random walk particle methods have been used to simulate full age distributions at points and in well screens in heterogeneous domains [Tompson *et al.*, 1999; Weissmann *et al.*, 2002]. These studies indicate that travel time distributions can be complex and often multimodal (non-Gaussian), even in samples of small aquifer volumes, such as from short-screened monitoring wells. Additional work is needed to study the effects of non-Gaussian dispersion on travel time distributions in a groundwater sample and to elucidate the effects of non-Gaussian distributions on apparent groundwater ages, reaction rates, and isotope fractionation effects.

[5] Existing studies have provided qualitative insights into the potential effects of mixing on apparent values of reaction rates and isotope fractionation parameters. Field studies of groundwater contaminant biodegradation indicate apparent isotope fractionation effects derived from environmental samples commonly are less pronounced than comparable isotope effects derived from measurements in homogeneous closed systems (e.g., laboratory experiments). Examples include N isotope fractionation during denitrification [e.g., Mariotti *et al.*, 1988; Smith *et al.*, 1991], C isotope fractionation during aerobic methyl tert-butyl ether degradation [Lesser *et al.*, 2008], O isotope fractionation during O₂ reduction [Revesz *et al.*, 1999], Cl and O isotope fractionation during perchlorate degradation [Hatzinger *et al.*, 2009], and Se isotope fractionation during selenate reduction [Clark and Johnson, 2008]. Denitrification provides a particularly useful test case for studying effects of mixing because original source concentrations can be estimated with relative ease from dissolved gas data. Mariotti *et al.* [1988] proposed that small apparent fractionation effects could be caused by sampling mobile water that was largely undenitrified but diluted by exchange with immobile water that was largely denitrified in dead-end pore spaces. Similar observations have been attributed qualitatively to heterogeneity in other aquifer studies without direct evidence or modeling support.

[6] Isotope fractionation during denitrification is characterized in this paper in terms of the parameter ε (sometimes called the “isotope enrichment factor”). This parameter is defined as $\varepsilon = \alpha - 1$, where α is a constant related to the instantaneous isotopic compositions of reacting NO₃⁻ and produced N₂ during denitrification according to

$$\alpha = (\delta^{15}\text{N}[\text{N}_2] + 1) / (\delta^{15}\text{N}[\text{NO}_3^-] + 1)$$

where

$$\delta^{15}\text{N} = \left[\left(\frac{^{15}\text{N}/^{14}\text{N}}{^{15}\text{N}/^{14}\text{N}} \right)_{\text{sample}} / \left(\frac{^{15}\text{N}/^{14}\text{N}}{^{15}\text{N}/^{14}\text{N}} \right)_{\text{air N}_2} - 1 \right], \quad \delta^{15}\text{N}[\text{N}_2]$$

is the $\delta^{15}\text{N}$ value of N₂, and $\delta^{15}\text{N}[\text{NO}_3^-]$ is the $\delta^{15}\text{N}$ value of NO₃⁻. Values of ε and $\delta^{15}\text{N}$ are small and are reported in parts per thousand (‰). Negative values of ε imply relative enrichment of ¹⁵N in residual NO₃⁻, whereas a value of 0 would imply no isotope fractionation.

[7] A few studies have addressed quantitatively the effects of mixing on estimated reaction rates and stable isotope fractionations in groundwater. For a single-continuum

one-dimensional system with simple boundary conditions and Gaussian dispersion, Kawanishi *et al.* [1993] showed with analytical solutions that the ratio of apparent to true values of ε ($\varepsilon_{\text{app}}/\varepsilon$) is a unique function of the ratio of the Damköhler number (*Da*) to the Peclet number (*Pe*). Abe and Hunkeler [2006] explored additional effects of transverse mixing on predicted values of ε and reaction progress derived from ε . These modeling studies of relatively simple systems indicate that dispersion can cause the apparent value of ε derived from groundwater samples to be substantially smaller than the intrinsic value (e.g., by as much as a factor of 2 for uniform longitudinal dispersion). More work is needed to determine the effects of physical heterogeneity in more realistically complex scenarios with, for example, geological heterogeneity, varying input concentrations, and reaction time lags due to inhibition of denitrification by dissolved O₂.

[8] The current study evaluates effects of mixing due to local dispersion and macroscopic physical heterogeneity on various parameter estimates for reactions and stable isotope fractionation associated with denitrification. For a heterogeneous aquifer in the San Joaquin Valley, California, experiments were conducted using simulated sample concentrations derived from calibrated numerical models of flow and reactive transport. Model calibration was conducted to provide a match between simulated and measured values of hydraulic head and concentrations of NO₃⁻, O₂, N₂ from denitrification, and atmospheric tracers CFC-12 and SF₆, and N isotope ratios in NO₃⁻. Calibrated reaction and fractionation parameters then were taken as the intrinsic or “true” values for the purpose of further numerical experiments in which “apparent” values were derived from simulated sample concentrations from short-screen observation wells. To evaluate controlling factors, physical and chemical attributes of the system were compared with ratios of apparent to true values of parameters, including the O₂ reduction rate, the O₂ concentration inhibiting denitrification, the NO₃⁻ reduction rate, and the N isotope fractionation parameter for denitrification. The ultimate objective of this study was to provide a context for rigorous interpretation of chemical and stable isotope data in complex geological systems.

2. Site Description and Data

[9] The study site is located in the eastern San Joaquin Valley, California, near the Merced River (Figure 1). Land use in this area is primarily agricultural. Previous studies demonstrated relatively large fluxes of NO₃⁻ in infiltrating unsaturated zone water and shallow groundwater [Domagalski *et al.*, 2008; Green *et al.*, 2008a, 2008b], resulting in elevated concentrations of NO₃⁻-N in the surficial aquifer, commonly above the maximum contaminant level (MCL) of 10 mg L⁻¹ set by the U.S. Environmental Protection Agency. Irrigation is supplied primarily by surface water diversions from reservoirs in the Sierra Nevada foothills. Groundwater is replenished by recharge below agricultural fields. The surficial aquifer is a mixture of coarse and fine alluvial fan sediments above a clay confining unit. The redox status of the unconfined groundwater ranges from aerobic to NO₃⁻ and Fe(III) reducing conditions. Electron donors in recharge water are scarce, and the redox reactions appear to be driven by relict, solid phase electron donors in the aquifer material such as organic carbon and

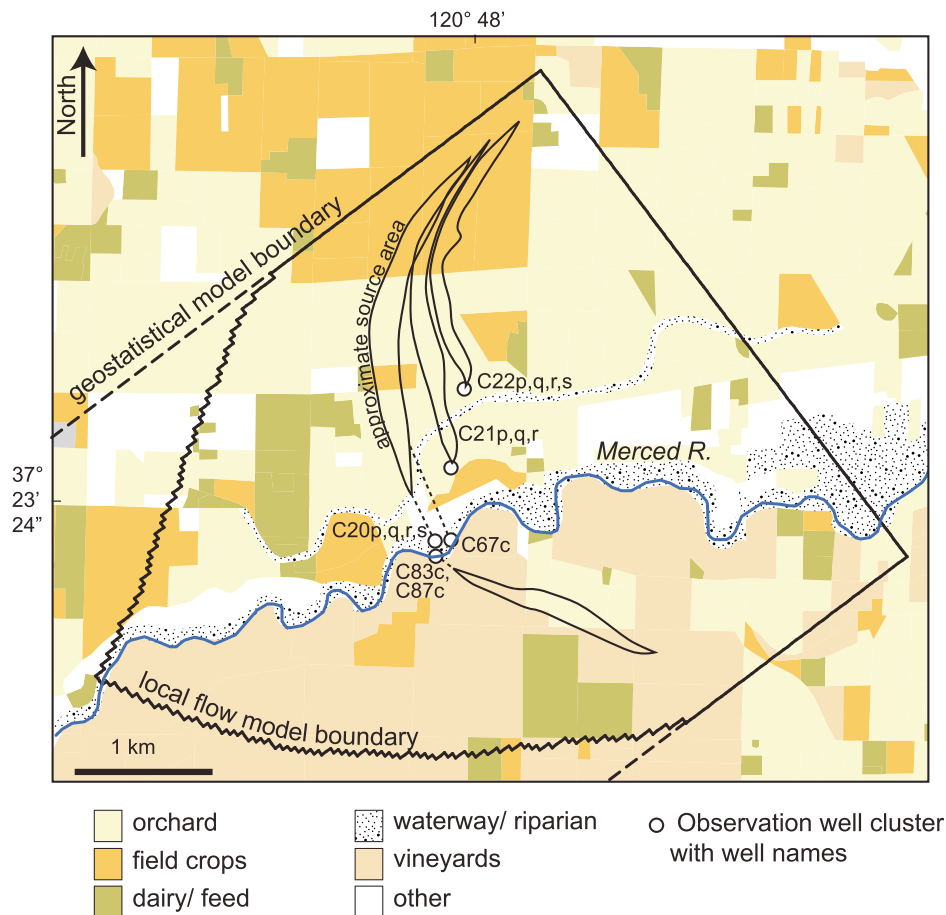


Figure 1. Site map, showing the boundaries of the local flow model, well nest locations, land use, and examples of approximate source area boundaries. Four wells (p, q, r, and s) were located at cluster C22, three wells were located at C21 (p, q, and r), and four wells were located at C20 (p, q, r, and s). Wells C83c/ C87c, and C67c were located on two separate river transects, each transect shown as a single point.

minerals containing reduced Fe and/or S [Green *et al.*, 2008a]. Additional aspects of the hydrogeology and geochemistry of the site are given elsewhere [Phillips *et al.*, 2007; Domagalski *et al.*, 2008; Green *et al.*, 2008a, 2008b].

[10] A 1 km transect of 11 nested monitoring wells was installed north of the Merced River at Delhi, California, in the summer of 2003 in cornfields and almond orchards (Figure 1). Monitoring wells were constructed of 5 cm diameter PVC with 60 cm long screens at depths of 8 to 30 m below ground surface. At the lower end of the 1 km transect, 20 PVC monitoring wells (5 cm diameter) were installed in or near the Merced River at depths of 0.3 to 2.8 m. Three of the 2.8 m depth wells with 15 cm screens were included in this study on the basis that the samples did not appear to be strongly influenced by surface water as indicated by major ion chemistry and did not appear to have degassed as indicated by dissolved gas analyses. Detailed descriptions of well installations, sampling, and analysis are given by Capel *et al.* [2008], Phillips *et al.* [2007], and Green *et al.* [2008a].

[11] Chemical and isotopic data were obtained from groundwater samples collected in late June and early July 2004 and were reported previously [Green *et al.*, 2008a]. Analyses used in this study include concentrations of NO_3^- , atmospheric age tracers, Ar, N_2 , and O_2 , and stable N isotope ratios in NO_3^- and N_2 . These analyses are described

briefly below. For additional information about analytical techniques and uncertainties, see Green *et al.* [2008a].

[12] Atmospheric age tracers sulfur hexafluoride (SF_6) and chlorofluorocarbons CFCl_3 (CFC-11), CF_2Cl_2 (CFC-12), and $\text{C}_2\text{F}_3\text{Cl}_3$ (CFC-113) were analyzed using electron-capture gas chromatography (<http://water.usgs.gov/lab/chlorofluorocarbons/>). Concentrations were converted to equivalent partial pressures in equilibrated air and compared with historic atmospheric concentrations [Busenberg and Plummer, 1992, 2000]. Concentrations of SF_6 were obtained for 11 transect wells and three streambed wells. Only one apparently reliable CFC-12 concentration was obtained for one transect well. Many CFC samples appeared to be contaminated or degraded. Age tracer concentrations were adjusted to account for dissolution of entrapped air bubbles, as indicated by dissolved gas analyses [Green *et al.*, 2008a].

[13] The concentrations and isotopic compositions of NO_3^- and N_2 were combined to assess NO_3^- sources and effects of denitrification [Vogel *et al.*, 1981; Heaton and Vogel, 1981; Böhlke *et al.*, 2002; Green *et al.*, 2008a]. Dissolved N_2 and Ar were analyzed by gas chromatography after creation of low-pressure headspace in the laboratory (<http://water.usgs.gov/lab/dissolved-gas/>). Concentrations of Ar and N_2 were used to estimate the quantities in groundwater of dissolved gases originating from atmospheric and biological sources, including “excess air” produced by

entrapped bubbles during recharge (assumed to be unfractionated) and “excess N_2 ” produced by denitrification. Degassing was not an important factor, based on estimates of excess air, sums of partial pressures of dissolved gases, and concentrations of atmospheric tracers that were consistent with containment of gases in solution. Concentrations of O_2 were measured in the field in a 50 mL flow-through cell, following stabilization of pH, specific conductance, and temperature. Stable N isotope ratios in N_2 were determined by gas chromatograph separation and continuous-flow isotope-ratio mass spectrometry (CFIRMS) on headspace gas (modified from *Revesz et al.* [1999]). Stable N isotope ratios in NO_3^- were determined by bacterial reduction to N_2O and CFIRMS [*Sigman et al.*, 2001].

3. Modeling Approach

[14] This study uses numerical modeling to examine the effects of mixing caused by local dispersion and macroscopic physical heterogeneity on apparent rates of reaction and isotopic fractionation derived from chemical and isotopic measurements. To estimate parameters that reasonably represented the processes at the field site, the flow, transport, and reactions were simulated in 3-D heterogeneous domains and calibrated to match model outputs of head, solute concentrations, and isotope data with observations from short-screen monitoring well samples. For further numerical experiments to examine mixing effects on reactions and stable isotope fractionations, the calibrated parameter values were taken as the intrinsic or “true” values. Common methods for analysis of field data were applied to the simulated well-sample concentrations to generate “apparent” reaction kinetic coefficients and ε values for comparison with the true parameter values. Ratios of apparent to true reaction rates and ε values were compared for increasingly complex scenarios by including or excluding variability of source concentrations, time lags in reactions, and effects of non-Gaussian dispersion. These methods are described in detail below.

3.1. Geological Models

[15] Two hundred realizations of the geology in the model study area were generated using the Transition Probability Geostatistics (TProGS) program [*Carle and Fogg*, 1996, 1997] to incorporate realistic 3-D heterogeneity of sedimentary hydrofacies. The model domain included a rectangular area of 24.6 km² and a depth of 55 m. Realizations were discretized at a scale of 40 m in the X- and Y-directions and 0.5 m in the Z-direction. Each realization included three main geological features: Holocene alluvium surrounding the Merced River, pre-Holocene alluvial fan sediments, and a basal clay confining layer (Figure 2a). Within these geological features, sediments were divided into subunits with similar hydraulic properties, or “hydrofacies” based on inspection of drillers’ logs and geophysical data. Hydrofacies included Holocene silt, silty sand, and sand, in the vicinity of the Merced River, and pre-Holocene clay, silt, silty sand, and sand in the surrounding alluvial fans. Observed geology at well locations was preserved in the realizations. Vertical transition probabilities and mean lengths were determined from drillers’ logs and geophysical logs. Horizontal dimensions were inferred from geological maps [*Marchand and Allwardt*, 1978, 1981] and from the dimensions of modern features, such as the river channel.

Estimated dimensions of hydrofacies are shown in Table 1. Mean lengths are generally 1 to 2 m in the vertical (Z) direction, 40 to 200 m in the strike (Y) direction, and 100 to 400 m in the dip (X) direction. Additional details are provided by *Phillips et al.* [2007].

3.2. Hydrologic Models

[16] All 200 realizations were ranked according to their domain-scale flow characteristics. Using MODFLOW2000 [*Harbaugh et al.*, 2000], the domain-scale hydraulic conductivity was calculated for each realization in the X, Y, and Z directions using simulations of flow with uniform hydraulic gradient in the direction of flow and no-flow boundaries on the sides of the model domain perpendicular to flow. Six representative realizations from the full set of 200 were selected for detailed study of transport and reactions. The six realizations were chosen to represent the ranges of domain-scale hydraulic properties (i.e., minimum, maximum, upper quartile, and median of $X + Y + Z$ flow), and indicators of anisotropy of domain-scale hydraulic properties (i.e., minimum and maximum of $((X+Y)/Z)$ flow). The total range of $X+Y+Z$ flow among realizations varied by 8%, and the range of the ratio of horizontal to vertical flow varied by 16%. The domain-scale flow characteristics of the different realizations are shown in Figures 2b and 2c.

[17] For the steady state flow models to simulate field conditions, hydraulic conductivity (K) values were either assigned to each of the four main hydrofacies (clay, silt, silty sand, sand) in all realizations on the basis of earlier parameter estimation [*Phillips et al.*, 2007] or were inversely modeled as discussed in section 3.4. On vertical faces of the local model domain used in this study, boundary fluxes were assigned by distributing fluxes from adjacent cells in a regional model as described by *Phillips et al.* [2007]. The flux assigned to each local model cell was weighted by the hydraulic conductivity of the cell. For all realizations, constant recharge to the water table was specified for individual farm fields on the basis of estimated crop demands and irrigation methods. Recharge rates varied from 0.15 m yr⁻¹ in unfarmed areas to 0.81 m yr⁻¹ in flood irrigated fields [*Phillips et al.*, 2007, Figure 18]. Although historical recharge values are not known for this site, atmospheric age tracers and N-species concentrations provided indications of historical hydrologic conditions that have affected transport. Calibration to these tracer data (see section 3.4) gave an estimate of steady state average hydrologic conditions over the time period of intensive agricultural use. Because irrigation was provided by surface water canals, groundwater pumping was not common in the shallow aquifer, and transient effects related to pumping were not significant.

3.3. Transport and Reaction Models

[18] Transport was simulated using a random walk particle tracking code, RWHet, for simulation of advection and local dispersion in heterogeneous media [*LaBolle et al.*, 2000]. Twenty thousand numerical particles, each representing a physical parcel of water in a well-sample, were introduced at each of 14 sampled well-screen locations (Figure 1) and backward tracked with random walk simulated dispersion and diffusion to the water table or local model boundaries. To simulate extracted groundwater samples, particle locations were assigned in well screens. Flux-weighted samples were

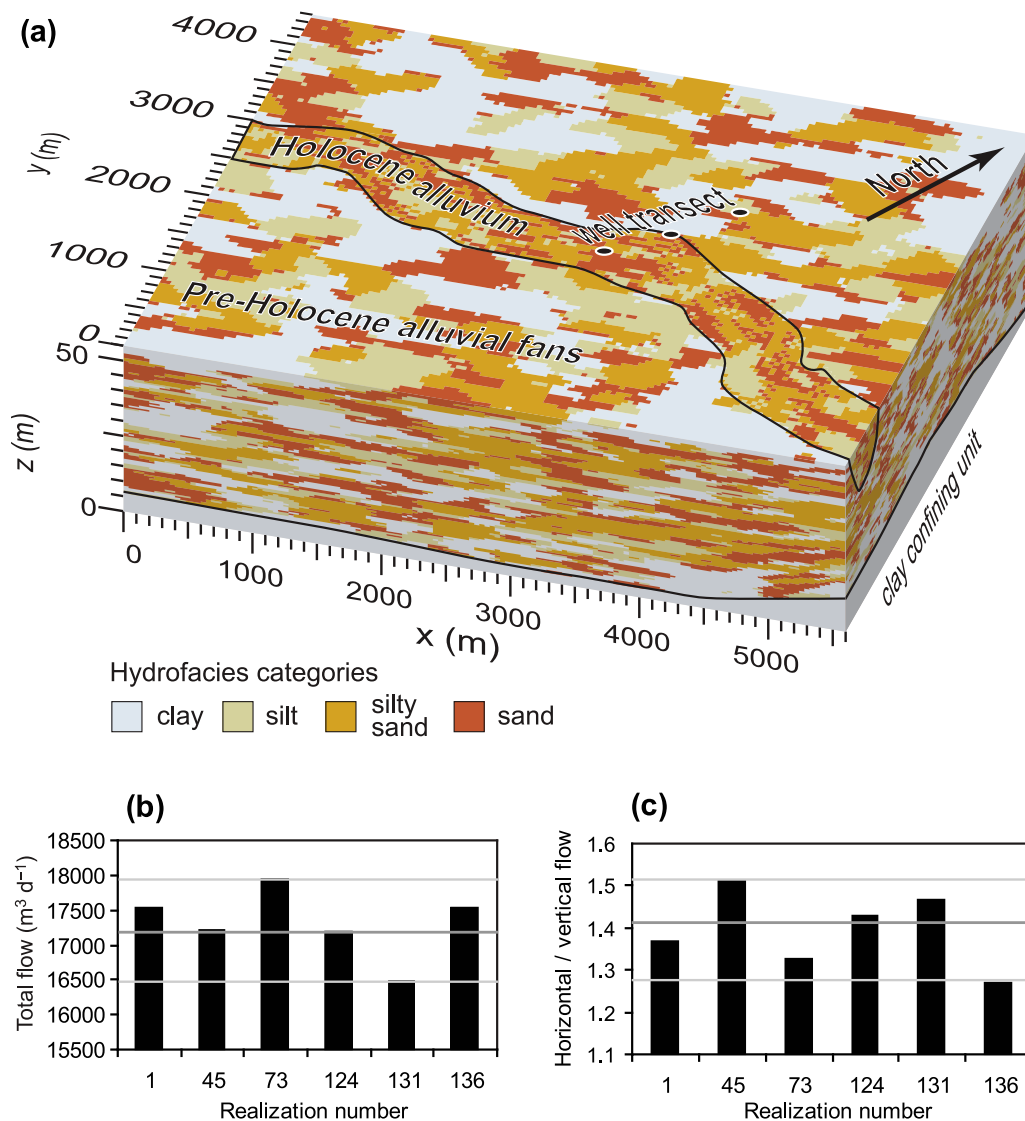


Figure 2. (a) Example geological realization. (b and c) Domain-scale hydraulic properties as characterized by flow simulations with simplified boundaries. Horizontal lines in Figures 2b and 2c show the median (dark gray) and minimum and maximum values (light gray) of 200 realizations.

estimated by specifying spatial density of particles in each layer to be proportional to the horizontal hydraulic conductivity of that layer. The age of each particle at the time of sampling was assigned as the travel time between the well screen and the water table. For a small number of particles that arrived at the local model boundary during backtracking, the total travel time was calculated as the advective-dispersive travel time to the boundary plane, plus an advective travel time from that boundary plane to the regional model water table. Advective travel times for the regional model were determined using MODPATH [Pollock, 1994]. The calculation of total travel time was done in a program module, described below. Such adjustments occurred for about 1–2% of the particles in the domain and did not strongly influence calculated concentrations or mean travel times.

[19] Simulated flux-weighted concentrations at the well screens were computed using a program module developed for this study. Concentrations of solutes associated with each particle at the time of recharge were assigned based on

the arrival time of the backward-tracked particle at the water table. The ensemble of particle travel times in a sample can be viewed as a distribution. Figure 3 shows a groundwater travel time distribution with typical complexity. Of 84 simulated samples, 65 showed multimodal distributions, and long-tailed distributions were common. Travel time distributions were highly variable for each well among differ-

Table 1. Proportions and Mean Lengths of Hydrofacies Used in Geostatistical Realizations

Geological Setting	Hydrofacies	Proportion	Mean Length, m		
			X	Y	Z
Holocene alluvium	silt	0.24	100	80	1.26
	silty sand	0.46	100	60	1.18
	sand	0.31	160	40	0.93
Pre-Holocene alluvial fan	clay	0.37	395	184	1.78
	silt	0.20	185	116	0.92
	silty sand	0.23	274	137	1.37
	sand	0.21	191	72	0.96

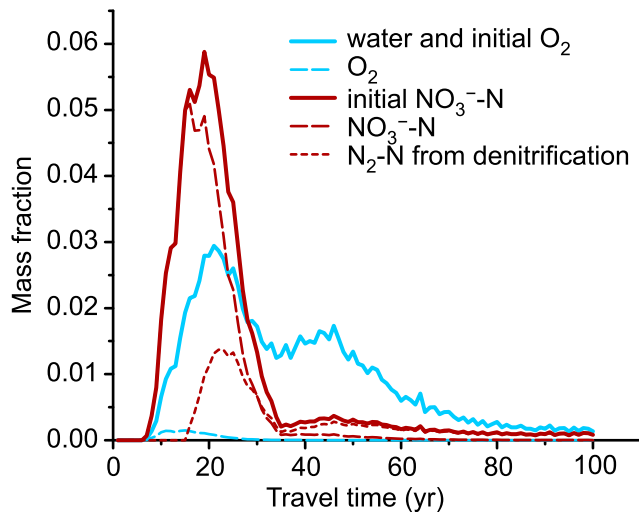


Figure 3. Travel time distribution of water and solute mass in the sample from C20q, realization 1. For solutes, mass fractions are with respect to the sum of initial O_2 or initial NO_3^- -N masses in all particles in the sample when they recharged. Bin size is 1 year.

ent realizations of geology, indicating that the particular shape was controlled by the geology upgradient of the well.

[20] Source concentrations at a particular time were uniform across the domain, and were either assigned based on a priori histories (for O_2 , SF_6 and CFC-12) or inversely modeled (for NO_3^- and $\delta^{15}N[NO_3^-]$). Source concentrations were assigned for all modeled constituents in each particle at the time of recharge. The recharge concentration of O_2 was set to a time-constant value for each well based on the equilibrium concentration (0.29 mmol L^{-1}) at the mean recharge temperature (19.2°C) and barometric pressure (101.07 kPa) estimated for this site, plus a quantity of O_2 from total dissolution of an entrapped excess air volume estimated for each well (mean O_2 in recharge of 0.34 mmol L^{-1}) [Green *et al.*, 2008a]. Input functions of SF_6 , CFC-12, and NO_3^- were piecewise linear in time. Recharge concentrations of SF_6 and CFC-12 were expressed as equivalent atmospheric mixing ratios in units of parts per trillion by volume (pptv) and were assigned to each particle based on the calculated value at equilibrium with the historical atmospheric concentrations at the time when the particle was at the water table [Busenberg and Plummer, 2000], plus contributions from excess air. Time varying, spatially uniform concentrations of NO_3^- and $\delta^{15}N[NO_3^-]$ in recharge were estimated using inverse modeling techniques, as described below. The uniform concentration of NO_3^- at the water table at a given time creates spatially variable NO_3^- fluxes, which are proportional to the local value of recharge. This assumption is consistent with unsaturated zone studies at this site [Nolan *et al.*, 2010] and at other sites [Nakamura *et al.*, 2004], which show increased fluxes of NO_3^- with increased water fluxes.

[21] The bulk concentration of a solute in a sample was calculated as the mean of concentrations associated with all particles in that sample,

$$[i] = \frac{1}{N} \sum_{p=1}^N [i]_p, \quad (1)$$

where $[i]$ is the bulk molar concentration of solute i , N is the number of particles, and $[i]_p$ is the molar concentration of solute i associated with particle p . Redox reactions were simulated with first-order decay and sequential use of terminal electron acceptors. Previous studies at this site demonstrate that redox reactions are driven mainly by solid phase electron donors [Green *et al.*, 2008a], and therefore the electron donor species were not included as mobile solutes. Concentrations of solutes associated with each particle at the well screen were computed based on the starting concentration at the water table and the reaction kinetic parameters. Sequential first-order decay of O_2 followed by NO_3^- was calculated for each particle with

$$[i]_p = [i]_{p,0} \exp(-k_i(t_p - t_{i-lag})), \quad \text{for } t_p > t_{i-lag}, \quad (2a)$$

$$[i]_p = [i]_{p,0} \quad \text{for } t_p \leq t_{i-lag}, \quad (2b)$$

where t_p is the travel time of the particle between the water table and the well screen, $[i]_{p,0}$ is the concentration at $t_p = 0$ (which is the time of recharge at the water table), k_i is the first-order rate constant, and t_{i-lag} is the time lag between recharge and the start of the reaction (e.g., due to inhibition of NO_3^- reduction by presence of O_2). The time lag for denitrification, t_{N-lag} is determined using

$$t_{N-lag} = \frac{\ln([O_2]_{cut}/[O_2]_0)}{-k_O} + t_{O-lag}, \quad (3)$$

where $[O_2]_{cut}$ is the molar concentration of O_2 at $t = t_{N-lag}$, i.e., a value of $[O_2]$ above which denitrification does not occur, and $[O_2]_0$ is the initial concentration of O_2 at the time of recharge. Field observations indicated a time lag close to zero for O_2 reduction, and so for simplicity t_{O-lag} was set to a constant value of zero.

[22] In aquifers, the dominant product of denitrification is N_2 , which allows use of the mass balance

$$[N_2-N]_{p,D} = [NO_3^-]_{p,0} - [NO_3^-]_p, \quad (4)$$

where $[N_2-N]_{p,D}$ is the molar concentration of excess N_2 (as N) produced by denitrification in particle p , $[NO_3^-]_{p,0}$ is the concentration of NO_3^- at the time of recharge, and $[NO_3^-]_p$ is the concentration of NO_3^- at the time of sampling. An example of the distribution of these N species with respect to travel time is shown in Figure 3. This mass balance was applied for each particle under the assumption that transport properties of all solutes were the same. Therefore, at any given travel time, the fractions of N in $[N_2-N]_D$ and $[NO_3^-]$ sum to the fraction of $[NO_3^-]_0$.

[23] Fractionation of stable isotopes during denitrification was calculated with a version of the Rayleigh fractionation equation

$$\delta^{15}N[NO_3^-]_p = \left(1 + \delta^{15}N[NO_3^-]_{p,0}\right) (f_{N,p})^\epsilon - 1, \quad (5)$$

where $\delta^{15}N[NO_3^-]_p$ is the isotopic composition of N in $[NO_3^-]$ associated with particle p , $\delta^{15}N[NO_3^-]_{p,0}$ is the isotopic composition of N in NO_3^- at the time of recharge, ϵ is

Table 2. Observation Groups and Optimization Parameters Used for Calibration

Observation Group Name	Number of Observations	Stage of Inversion	Median Observation Error (Standard Deviation)	Parameters Estimated From Observations
Hydraulic heads	11	1	0.87 m	K , ^a por, ^b disp, ^c rchg ^d
SF ₆	15	1	0.69 pptv	K , por, disp, rchg
CFC-12	1	1	26.11 pptv	K , por, disp, rchg
[O ₂]	14	2, 3	10 $\mu\text{mol L}^{-1}$	ε , k_N , k_O , [O ₂] _{cut}
$k_{O,app}$	14	2, 3	0.089 yr ⁻¹	ε , k_N , k_O , [O ₂] _{cut}
[NO ₃]	14	2, 3	29 $\mu\text{mol L}^{-1}$	ε , k_N , k_O , [O ₂] _{cut}
[NO ₃] ₀	14	2	30 $\mu\text{mol L}^{-1}$	input [NO ₃] ₀ , input $\delta^{15}\text{N}[\text{NO}_3]_0$
$f_{N,p}$	14	2, 3	0.089	ε , k_N , k_O , [O ₂] _{cut}
$\delta^{15}\text{N}[\text{NO}_3]$	14	2, 3	0.54‰	ε , k_N , k_O , [O ₂] _{cut}
$\delta^{15}\text{N}[\text{NO}_3]_0$	9	2	1.9‰	input [NO ₃] ₀ , input $\delta^{15}\text{N}[\text{NO}_3]_0$
ε_{app}	6	2, 3	3.61‰	ε , k_N , k_O , [O ₂] _{cut}

^aHydraulic conductivity (K) estimates include vertical K of clay hydrofacies and underlying clay layer and horizontal K of sand hydrofacies.

^bPorosity (por) was assumed to be uniform.

^cDispersivity (disp) was assumed to be uniform and isotropic.

^dSpatially varying recharge values from Phillips *et al.* [2007, Figure 18] were multiplied by a constant scale factor (rchg).

the isotope fractionation parameter ($\varepsilon = \alpha - 1$), and $f_{N,p}$ is the fraction of NO₃⁻ remaining, defined by

$$f_{N,p} = [\text{NO}_3^-]_p / [\text{NO}_3^-]_{p,0}. \quad (6)$$

Reactions proceeded in each particle independently according to equations (2)–(6). While it is likely that spatial variability of electron donors in the aquifer resulted in different rates of reaction within different lithologic units, reaction kinetics were assumed to be spatially uniform in the current study to maintain numerical efficiency and to highlight the effects of geological heterogeneity in the absence of reactivity contrasts.

3.4. Parameter Estimation

[24] Automated parameter estimation was used to obtain realistic reactive transport scenarios to be used for subsequent numerical experiments. The flow and reactive transport models were calibrated using PEST [Doherty, 2008], a numerical code for nonlinear parameter estimation. The calibration procedure was designed to give a reasonable fit of model output to observed reactive trends (such as the commonly reported change in $\delta^{15}\text{N}[\text{NO}_3^-]$ versus f_N) as well as sample concentrations. Model parameters were adjusted to minimize the discrepancies between modeled and measured concentrations, stable isotope ratios, and apparent sample values of $f_{N,app}$, $k_{O,app}$, and ε_{app} (Table 2). For models and field observations, the apparent values of $f_{N,app}$, $k_{O,app}$, and ε_{app} were computed using bulk sample concentrations in place of particle concentrations in equations (6), (2), and (5), respectively.

[25] Sensitivity tests indicated that noise in computed derivatives of stable isotope ratios prevented simultaneous inversion of transport and reaction parameters. Noisy derivatives of the stable isotope ratios with respect to flow and transport parameters resulted from use of the random walk method. Although noise diminished with increasing numbers of numerical particles, it could not be eliminated with the available computational resources. To avoid the effects of noise on calibration, a multiple-stage parameter estimation approach was used with transport parameters estimated separately from reaction parameters (Table 2). First, hydraulic and transport parameters were estimated by minimizing the error between modeled and measured observa-

tions of hydraulic head and age tracer concentrations. These parameters included hydraulic conductivities (K) of hydrofacies, uniform porosity (θ), uniform isotropic dispersivity (α), and a multiplication factor for the spatially varying recharge (Table 3). On the basis of previous sensitivity analyses [Phillips *et al.*, 2007], K values selected for recalibration included vertical K (K_v) of the clay hydrofacies, K_v of the underlying clay layer, and horizontal K (K_h) of sand. For other values of hydraulic conductivity of sediment classes, previously estimated values were held constant at K_h silty sand = 30 m d⁻¹, K_h silt = 8 m d⁻¹, K_h clay = 0.3 m d⁻¹, K_v sand = 40 m d⁻¹, K_v silty sand = 6 m d⁻¹, and K_v silt = 1 m d⁻¹. In the second stage of parameter estimation, source concentration input functions were determined for [NO₃]₀ and $\delta^{15}\text{N}[\text{NO}_3]_0$ by assuming linear variation between estimated values in years 2005, 1995, 1985, 1965, 1945, 1925, 1905, and 1867. Regularization was used to minimize noise in the input functions [Doherty, 2008]. The source concentrations were adjusted along with reaction parameters to match observed with simulated values of [NO₃]₀ and $\delta^{15}\text{N}[\text{NO}_3]_0$ in samples. Third, to simplify comparison among realizations, reaction parameters were reestimated by using the mean of the stage-two input functions as a single input function for all realizations (Figure 4). Using the averaged input functions resulted in a minor increase of standard error of weighted-residuals of 8%. In the third stage, reaction parameters k_O , [O₂]_{cut}, k_N , and ε , were adjusted to minimize the error between modeled and observed values of [O₂], [NO₃], $k_{O,app}$, $f_{N,app}$, and ε_{app} .

[26] In the parameter estimation routine, observation weights were assigned on the basis of estimated errors for each observation derived from an error propagation analysis (Table 2). For each observation, the weight was equal to the inverse of the observation error, as recommended, for example, by Doherty [2008].

4. Results and Discussion of Parameter Estimation

[27] Estimated parameter values are shown in Table 3 and Figure 4. Although these estimates were generated primarily to provide a basis for further numerical experiments and are not the focus of the current work, certain results warrant mentioning. The mean input values of $\delta^{15}\text{N}[\text{NO}_3]_0$ and

Table 3. Calibrated Flow, Transport, Reaction, and Chemical Source Parameters for Six Representative Realizations, and Peclet and Damköhler Numbers

	Geological Realization Number					
	1	45	73	124	131	136
<i>Fit Parameters From Inverse Modeling</i>						
Dispersivity (m)	0.008	0.024	0.015	0.015	0.064	0.031
Porosity	0.380	0.380	0.380	0.381	0.380	0.380
K_v base ^a (m d ⁻¹)	5.9×10^{-6}	5.6×10^{-6}	6.1×10^{-7}	9.0×10^{-6}	5.2×10^{-6}	2.3×10^{-5}
K_h sand ^b (m d ⁻¹)	155.5	61.6	36.6	39.9	76.3	20.0
K_v clay (m d ⁻¹)	0.22	0.45	0.45	0.45	0.14	0.28
Recharge ^c	0.98	0.72	0.69	0.67	0.71	0.45
ε (‰)	-27	-18	-34	-16	-37	-25
k_N (yr ⁻¹)	0.046	0.032	0.35	0.033	0.031	0.12
k_O (yr ⁻¹)	0.17	0.16	0.15	0.13	0.19	0.15
$[O_2]_{cut}$ (μmol L ⁻¹)	26	50	9	50	9	18
<i>Secondary Parameters Calculated From Model Results</i>						
Pe	18.6 ^d (2.5–31.3)	19.1 (4.5–28.8)	30.5 (4.2–55.1)	20.4 (3.9–38.1)	15.9 (2.6–41.1)	15.7 (2.9–42.1)
Da_{O_2}	5.7 (0.4–10.5)	6.2 (1.1–11.4)	5.6 (0.5–15.3)	5.3 (0.4–10.6)	7.8 (1.1–15.6)	8.4 (1–24.4)
Da_{NO_3}	1.6 (0.1–2.8)	1.2 (0.2–2.3)	13.5 (1.1–37.1)	1.3 (0.1–2.6)	1.3 (0.2–2.5)	6.6 (0.8–19.1)

^aVertical hydraulic conductivity of the basal clay layer below the active flow domain with general head boundaries.

^bHorizontal hydraulic conductivity of sand hydrofacies in the active flow domain.

^cRecharge given as a fraction of fluxes applied in the previous model calibrated to hydraulic heads [Phillips et al., 2007, Figure 18].

^dMedian value from all wells in the geological realization and, in parentheses, the range of values for individual wells.

$[NO_3^-]_0$ at the water table are feasible given the land use histories in the study area (Figure 4). The input function of $[NO_3^-]_0$ has a steep increase in modern fluxes, consistent with post-World War II use of chemical fertilizers (Figure 4a). The increased use of chemical fertilizers tends to cause a decrease in $\delta^{15}N[NO_3^-]_0$, which is seen in the mean modeled input values in Figure 4b. Elevated values of $\delta^{15}N[NO_3^-]_0$ at early times are consistent with manure sources of N, which were common during the early agricultural history of the area [Green et al., 2008b], and might also indicate components of natural NO_3^- [e.g., McMahon and Böhlke, 2006]. Recharge values for these simulations calibrated using water levels and age tracers were 0.45 to 0.98 times the previously estimated values based on calibration with recent (2003–2005) water levels only [Phillips et al., 2007]. The current numerical models calibrated to age tracer concentrations likely represent a steady state average of historical hydrology, because the distribution of age tracer concentrations is controlled by hydrologic conditions from the time of recharge to the time of sampling.

[28] Simulated age tracer concentrations and chemical gradients from calibrated model outputs for the six realizations are compared with observed values in Figure 5. On scatterplots of modeled versus observed values (Figures 5a to 5f), points are clustered around the 1:1 line, indicating that simulated physical and chemical processes reasonably represent the natural system, though with considerable scatter. For comparison of modeled and measured apparent reaction trends, model-derived results for individual samples are compared with measured values on plots showing O_2 reduction progress ($\ln(f_O)$) versus SF_6 -derived apparent age, Figure 5g) and change in isotopic composition of NO_3^- ($\Delta\delta^{15}N[NO_3^-]$ versus f_N , Figure 5h). For apparent reaction trends, the model output follows the minimum-error path through the center of observed data. Model results are more closely clustered than the observed data, indicating greater temporal and/or spatial variability, and/or measurement uncertainties, in the real system than in the model.

[29] The effect of different geological realizations on parameter estimates was minor relative to the uncertainty in the parameter estimates. For all parameters, the estimated 95% confidence limits overlapped among all six simulations (not shown), with the exception of k_N in simulation 73.

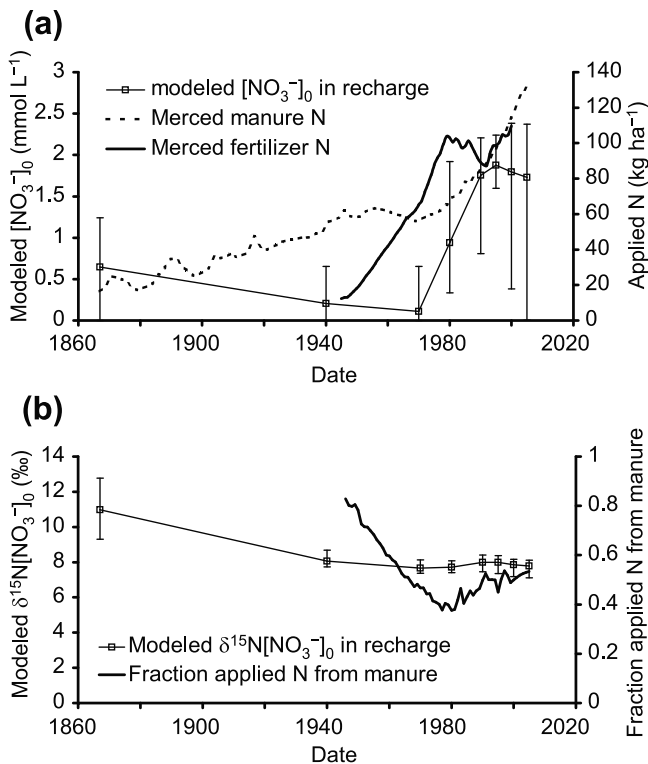


Figure 4. Calibrated model parameters of (a) $[NO_3^-]_0$ and (b) $\delta^{15}N[NO_3^-]_0$ in recharge over time, compared with reported county-wide application rates of manure N and fertilizer N [Green et al., 2008b]. Other sources of NO_3^- also may have been present. The points show the means, and the vertical bars show the total range of values from six simulations.

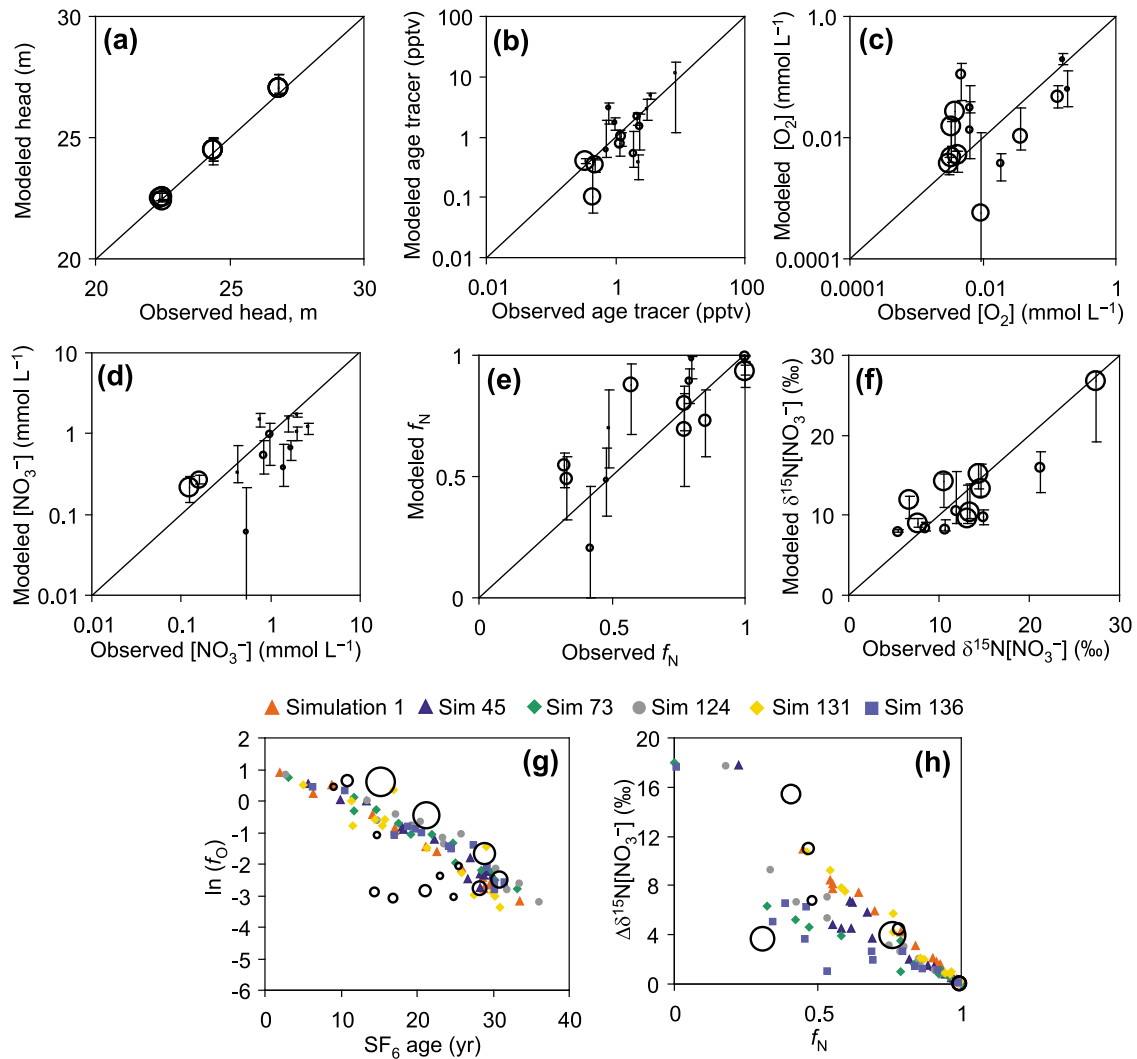


Figure 5. Comparison of modeled and measured values of (a) head, (b) age tracers including SF_6 and CFC-12, (c) $[O_2]$, (d) $[NO_3^-]$, (e) apparent f_N , (f) $\delta^{15}N[NO_3^-]$, (g) trends in f_O versus SF_6 -derived apparent age, and (h) change in N isotopic composition of NO_3^- ($\Delta\delta^{15}N[NO_3^-] = \delta^{15}N[NO_3^-] - \delta^{15}N[NO_3^-]_0$) versus f_N . Open circles show the median of modeled values, and the size of the circle is proportional to the weight applied to that observation in the inversion. Vertical bars show the total range of modeled values from six simulations. In Figures 5g and 5h, points indicate modeled values for 14 individual well screens in each simulation.

Because of the inherent uncertainty of the parameter estimates, further numerical experiments consider ranges of parameter values in addition to the calibrated values.

5. Results and Discussion of Numerical Experiments

5.1. Estimation of Apparent k_O , k_N , $[O_2]_{cut}$, and ϵ

[30] Using the calibrated transport and reaction simulations, numerical experiments were conducted to compare true and apparent values of reaction kinetic parameters (k_O , k_N), oxygen cutoff for denitrification ($[O_2]_{cut}$), and the N isotope fractionation parameter for denitrification (ϵ). Apparent values of the parameters were calculated using simulated sample concentrations from the 14 observation wells. The true values were the calibrated parameter values

in the numerical models used to generate the simulated samples. Apparent k_O ($k_{O,app}$) and apparent k_N ($k_{N,app}$) were calculated using both mean particle travel times and apparent ages derived from simulated SF_6 concentrations, as both approaches are relevant to previous modeling and field studies. Values of apparent k_O ($k_{O,app}$) and apparent ϵ (ϵ_{app}) were calculated for individual simulated samples by substituting concentrations obtained with equation (1) into equations (2a) and (5) (Figures 6a and 6d). For solutions of $k_{N,app}$ and $[O_2]_{cut,app}$, the information available from a single sample is not sufficient to determine a unique value. Therefore each value of $k_{N,app}$ and $[O_2]_{cut,app}$ was estimated once for each simulation using linear regression methods applied to the set of 14 samples from that simulation. To solve for $[O_2]_{cut,app}$, simulated values of $\ln(f_N)$ were plotted against $\ln(f_O)$ (Figure 6b inset) to produce a theoretical linear trend

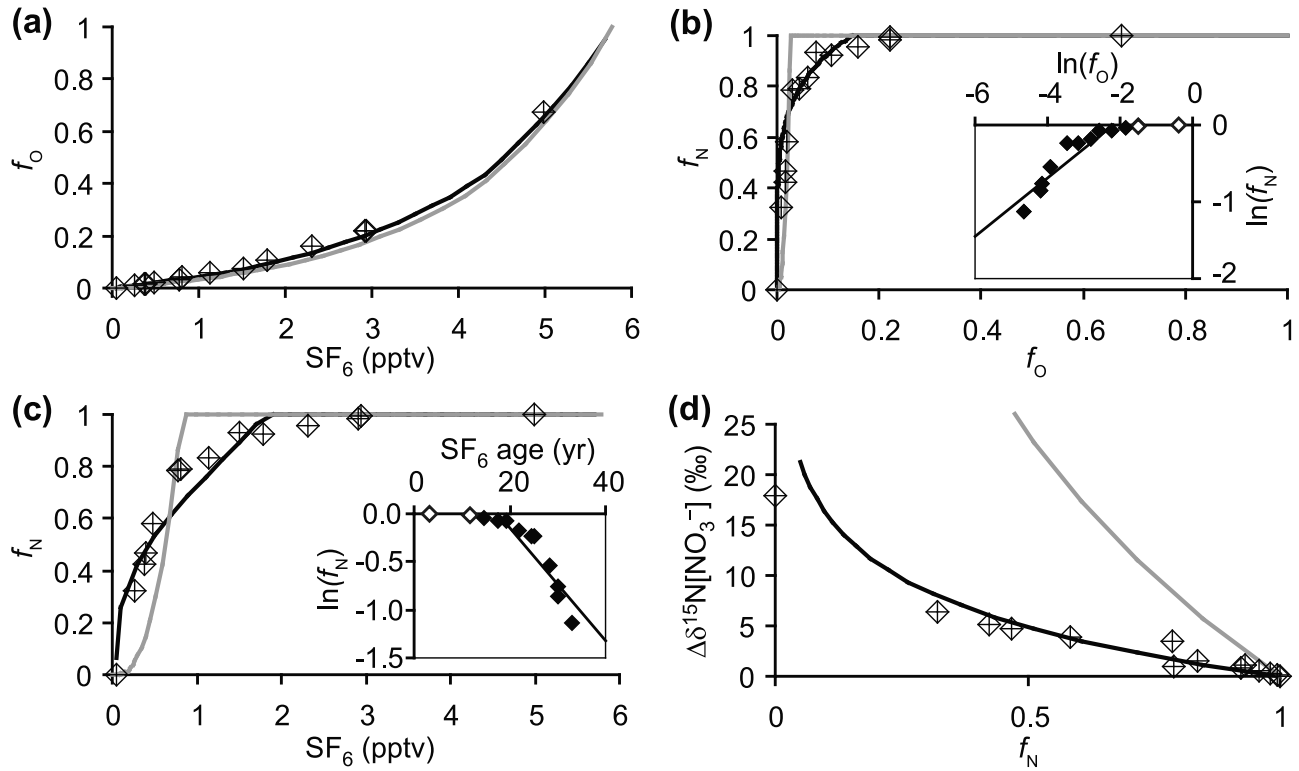


Figure 6. Example comparisons from simulation 73 of piston flow trends derived from apparent and true parameters (lines) to simulated sample concentrations (points) for (a) O_2 reduction, (b) transition from O_2 reduction to NO_3^- reduction, (c) NO_3^- reduction, and (d) N isotope fractionation ($\Delta\delta^{15}N[NO_3^-] = \delta^{15}N[NO_3^-] - \delta^{15}N[NO_3^-]_0$). In all plots, gray curves are trends predicted by assuming piston flow but using the true parameter values. The black curves are piston flow trends based on the apparent parameters. On inset log-scale plots, the trend lines are the linear least squares best fits to the simulated data (points) used to estimate the apparent parameter value. Empty points are excluded from the regression because f_N is approximately 1 (>0.98).

with intercept on the $\ln(f_O)$ axis of $\ln([O_2]_{cut}/[O_2]_0)$ according to

$$\ln(f_O) = \frac{k_O}{k_N} \ln(f_N) + \ln\left(\frac{[O_2]_{cut}}{[O_2]_0}\right), \quad (7)$$

where f_O is equal to $[O_2]/[O_2]_0$, and f_N is equal to $[NO_3^-]/[NO_3^-]_0$. Equation (7) was obtained by combining equations (2a) and (3). To solve for $k_{N,app}$, linear least squares regression was applied to a plot of $\ln(f_N)$ versus mean particle travel time or simulated SF_6 -derived apparent age (equation (3a), Figure 6c inset), with $k_{N,app}$ determined from the slope of the regression line. Limitations of the apparent-parameter estimation techniques are evident in the nonlinearity of simulated concentration trends (points). Although the linearity assumptions of these methods are consistent with the equations used to simulate the sample concentrations, nonlinearities result from the mixing of aerobic water with no denitrification ($f_N = 1$) with anaerobic water with active denitrification, as in real samples.

[31] To illustrate how apparent parameter values were estimated for numerical experiments, and to clarify the differences between true and apparent parameters, Figures 6a, 6b, 6c, and 6d show simulated tracer concentrations in wells (points) along with trends (curves) based on true and apparent reaction and fractionation parameters for simula-

tion 73 (Table 3). True parameters are from parameter estimation (section 3.4) which yielded the simulated concentrations shown in Figure 6. Apparent parameters are estimated as described above based on the simulated tracer concentrations. The trends are derived by substituting parameters directly into the reaction and fractionation equations (2)–(6) and are referred to as “piston flow trends” in reference to the common assumption that water and solutes in a groundwater sample are transported as a discrete package with a single input concentration of each constituent and a single travel time. As expected, the estimated trends from apparent parameters appear consistent with the simulated concentrations from which they were derived. The piston flow trends for true parameters are not used further in this study, but are shown here to illustrate the basic differences between true and apparent parameter estimates. The different trends produced by true and apparent parameters show that the apparent reaction kinetic coefficients derived from concentrations of samples are systematically different from the true values. For example, ε_{app} tends to be closer to zero than ε , as shown by the lower slope of the trend derived from apparent parameters on Figure 6d, and as previously reported by Kawanishi *et al.* [1993]. However, the relative effects vary among parameters, as shown by a small difference between trends for O_2 consumption (Figure 6a), and

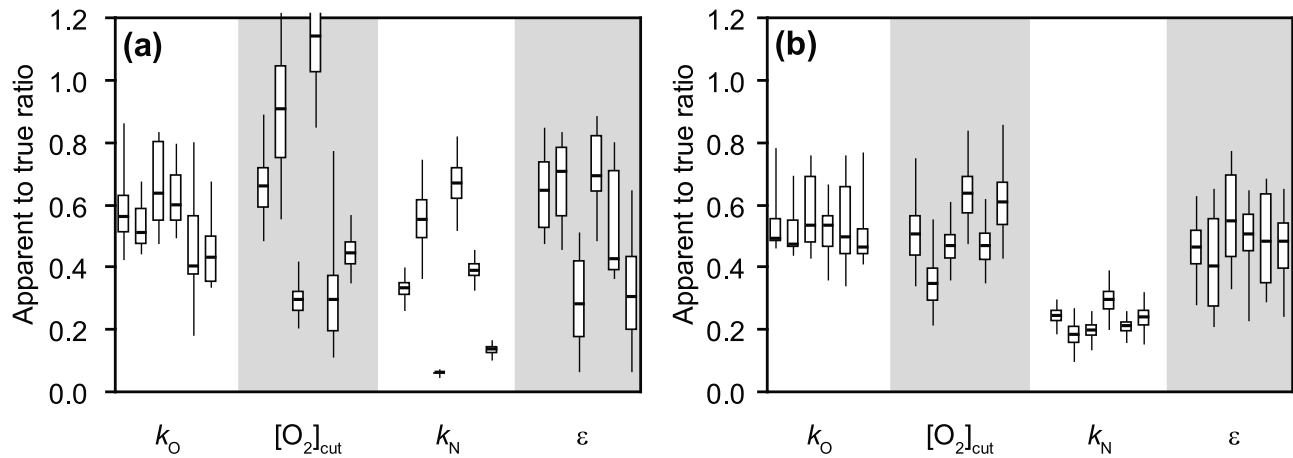


Figure 7. Ratios of apparent to true values of O_2 reduction rate (k_O), O_2 cutoff value ($[O_2]_{cut}$), NO_3^- reduction rate (k_N), and isotope fractionation parameter (ϵ) as predicted by (a) individually calibrated simulations with true values shown in Table 3 and (b) forward simulation using a single set of parameter values for all six geological scenarios with each parameter equal to the mean of values from individual scenarios. For each of the six simulations, the distribution of results from individual well samples is shown as a box plot with bold horizontal line showing the median, box showing the interquartile range, and whiskers showing the total range. Simulations are ordered 1, 45, 73, 124, 131, to 136, left to right for each parameter. For $[O_2]_{cut}$ and k_N , which were estimated using linear least squares regression, the interquartiles are $0.674 \times$ standard error, and the ranges are two times the standard error. The k_O and k_N values were computed with respect to the mean particle travel time for each well sample.

a larger difference between trends for N isotope fractionation (Figure 6d).

5.2. True Versus Apparent k_O , k_N , $[O_2]_{cut}$, and ϵ

[32] To show the effects of geological heterogeneity on parameter estimates, ratios of apparent to true k_O , k_N , $[O_2]_{cut}$, and ϵ were compared among the calibrated simulations and among simulations using identical transport and reaction parameters. In the latter case, parameter values were set equal to the mean of the calibrated parameter values (Table 3), so the only difference among simulations was the underlying geological realization. The median, quartiles, and ranges of the ratios of apparent to true parameter values are shown in Figure 7a for calibrated simulations and Figure 7b for simulations with identical parameters. Values of $k_{N,app}$ and $k_{O,app}$ were computed with respect to the mean particle travel time of each sample

[33] Ratios of apparent to true values were variable among individually calibrated simulations and among individual wells within each realization. Among calibrated simulations, the large variability of the ratio of apparent to true $[O_2]_{cut}$, k_N , and ϵ (Figure 7a) mainly resulted from uncertainty in the parameter estimation process and was not directly produced by model domain-scale differences in geology. This is indicated by the relatively small variability of medians of $k_{O,app}/k_O$, $[O_2]_{cut,app}/[O_2]_{cut}$, $k_{N,app}/k_N$, and ϵ_{app}/ϵ among simulations with the same flow, transport, and reaction parameters but with different geological realizations (Figure 7b). Below the scale of the model domain, however, local geological variability produced large differences among individual wells within a single realization. This is shown by the ranges of whiskers on individual box-plots for k_O and ϵ in both Figures 7a and 7b. For example, the $k_{O,app}/k_O$ ratio in realization 131 might range from 0.2 to 0.8 for

any randomly chosen well. Among wells in a single aquifer, variability of apparent rates can result solely from differences among the sedimentary networks through which solutes travel to each well. Similarly, multiple realizations of these networks for a single well can result in a wide range of apparent reaction and fractionation parameters.

[34] Model domain-scale differences in flow characteristics (Figures 2b and 2c) showed some limited correlations with the ratio of apparent to true reaction and fractionation parameters. It was hypothesized that realizations with higher ratios of horizontal to vertical domain-scale flow (i.e., stronger domain-scale anisotropy) have greater tortuosity of flow paths between the water table and well screens, greater mixing, and greater differences between apparent and true parameters. For realizations 45 and 131, the strong contrasts between horizontal and vertical flows did correspond with low ratios of apparent to true parameter values (Figure 7b). In other cases, there was no clear correspondence between domain-scale flow properties and mixing effects. Realization 124 had median flow properties and close-to-median anisotropy, yet yielded the highest medians of $k_{O,app}/k_O$, $[O_2]_{cut,app}/[O_2]_{cut}$, and $k_{N,app}/k_N$. In cases such as this, local geological features that control mixing along the flow paths between the water table and the well screens likely differ from more widely distributed features that control the overall domain-scale flow properties.

[35] The comparison of $[O_2]_{cut,app}$ with $[O_2]_{cut}$ (Figure 8) has relevance to previous laboratory and field studies of denitrification inhibition by O_2 . The threshold value of $[O_2]_{cut}$ required for the onset of denitrification is variable and dependent on multiple factors such as composition of the microbial community, sediment environmental factors, and molecular-level processes [Conrad, 1996; Zumft, 1997]. Although some laboratory data indicate relatively high limits [e.g., Chen *et al.*, 2003], in homogeneous laboratory

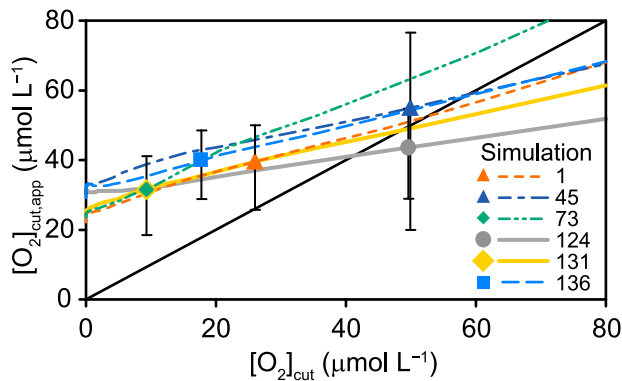


Figure 8. Comparison of true model $[O_2]_{\text{cut}}$ to $[O_2]_{\text{cut,app}}$ for calibrated simulations (points) and for the same simulations with ranges of $[O_2]_{\text{cut}}$ values assigned in place of the optimal $[O_2]_{\text{cut}}$ (curves). Error bars show \pm two standard deviations. The diagonal black line is 1:1.

systems, $[O_2]_{\text{cut}}$ commonly is observed to be between about 0 and $10 \mu\text{mol L}^{-1}$ [Tiedje, 1988; Seitzinger *et al.*, 2006; Coyne, 2008]. In contrast, $[O_2]_{\text{cut,app}}$ values derived from analyses of groundwater samples in aquifer redox gradients commonly are around 40 to $60 \mu\text{mol L}^{-1}$ [Böhlke *et al.*, 2002; McMahon *et al.*, 2004; Böhlke *et al.*, 2007; Green *et al.*, 2008a].

[36] Our study indicates that low values of $[O_2]_{\text{cut}}$ commonly observed in the laboratory would not be detectable in mixed groundwater samples because mixtures of travel times in samples create the appearance of denitrification in the presence of relatively high concentrations of O_2 . Figure 8 shows comparisons of $[O_2]_{\text{cut,app}}$ to $[O_2]_{\text{cut}}$ for each geological realization (points) and for the same scenarios with ranges of $[O_2]_{\text{cut}}$ values assigned in place of the optimal $[O_2]_{\text{cut}}$ (colored curves). Among the six realizations, points lie along an approximately linear trend with $[O_2]_{\text{cut,app}}$ ranging from 30 to $50 \mu\text{mol L}^{-1}$ while calibrated $[O_2]_{\text{cut}}$ ranges from 9 to $50 \mu\text{mol L}^{-1}$. As $[O_2]_{\text{cut}}$ approaches zero, $[O_2]_{\text{cut,app}}$ remains greater than $24 \mu\text{mol L}^{-1}$ for all realizations. Therefore previously reported $[O_2]_{\text{cut,app}}$ values of approximately $50 \mu\text{mol L}^{-1}$ may be the result of inhibition of denitrification at lower concentrations of O_2 along with mixing during transport and sampling. An apparent value of $[O_2]_{\text{cut,app}} < 40 \mu\text{mol L}^{-1}$ obtained from sample analyses is consistent with actual onset at $[O_2]_{\text{cut}} < 10 \mu\text{mol L}^{-1}$.

5.3. Factors Affecting Apparent k_O , k_N , and $[O_2]_{\text{cut}}$

[37] For simple scenarios with Gaussian dispersion, Kawanishi *et al.* [1993] showed that the ratio $\varepsilon_{\text{app}}/\varepsilon$ is related to the ratio of the Damköhler number (Da , relating the time scales of reaction and advection) to the Peclet number (Pe , relating the rates of advection and dispersion). Our study extends their analysis to reaction rates and explores additional effects of non-Gaussian mixing, time-varying source concentrations, and time lags of reaction rates for realistic simulations of a heterogeneous aquifer.

[38] For each of the six calibrated simulations and for additional test cases, ratios of apparent to true values were compared with estimates of Da/Pe . Values of Pe were estimated for individual well samples in all realizations. For

each well, an effective dispersion coefficient was estimated using

$$D_L = \frac{\sigma_{x_p'}^2}{2\bar{t}} \quad (8a)$$

$$x_p' = \frac{x_p}{t_p} \bar{t}, \quad (8b)$$

where D_L is the effective longitudinal dispersion coefficient of the portion of the aquifer through which particles traveled to the well screen, \bar{t} is the mean of travel times, t_p , between the water table and well screen for all particles in the well, and $\sigma_{x_p'}^2$ is the variance of normalized travel distances, x_p' , at time \bar{t} (equation (8b)). Travel distance, x_p , is normalized to account for particles intersecting the water table across a wide range of times and locations. An effective Peclet number was calculated for each well using

$$Pe = \frac{\bar{x}' \bar{v}}{D_L}, \quad (9)$$

where \bar{x}' is the mean normalized travel distance and \bar{v} is the mean of particle velocities which are equal to the ratio x_p/t_p . Effective Damköhler numbers were calculated for O_2 (Da_O) and NO_3^- (Da_N) at each well using

$$Da_i = k_i \bar{t} \quad (10)$$

where Da_i is the Damköhler number for solute i , and k_i is the first-order reaction rate. Da/Pe ratios were computed for each well. Composite, aquifer-scale Pe , Da_O , and Da_N values were computed as the medians of the Pe and Da values for individual wells. To characterize Da_N for each simulation, only those wells included in the linear regression to determine $k_{N,app}$ (e.g., filled points on inset graph in Figure 6c) were included in statistics.

[39] For apparent reaction rates and isotope fractionations, the effects of mixing are closely tied to the scale of transport to individual wells. For each well, Figure 9a shows values of macroscopic effective dispersivity, α_L , calculated using

$$\alpha_L = \frac{D_L - D^*}{\bar{v}}, \quad (11)$$

where D^* is the effective diffusion coefficient and is assumed to be negligible in this case. The increase of α_L with increasing transport distance at a slope of approximately 0.1 is consistent with previous studies showing this relationship in field measurements at comparable scales [Gelhar, 1986]. As the scale of transport and α_L increase, $\varepsilon_{\text{app}}/\varepsilon$ decreases (Figure 9b) as do the ratios of apparent to true reaction coefficients (not shown). Therefore physical mixing tends to create the appearance of lower reaction rates and fractionation parameters when measured at larger scales and longer flow paths (Figure 9b). The scale effect may contribute to previous observations that rates of denitrification tend to be higher for smaller-scale push-pull tests as compared with larger scale aquifer studies [Smith *et al.*, 2004; Green *et al.*, 2008a]. The effects of transport and scale should be considered when comparing reaction rates in different aquifer systems, or when comparing reaction rates in different parts of the same system.

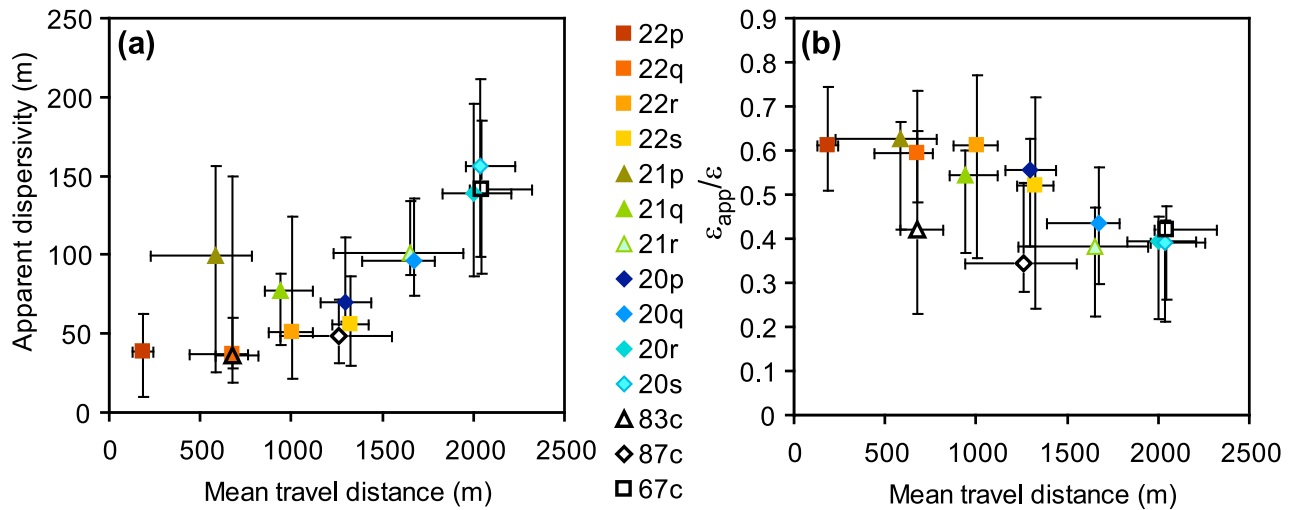


Figure 9. Comparison of (a) macroscopic dispersivity from equation (11) and (b) $\varepsilon_{app}/\varepsilon$ to mean travel distance for the 14 wells. For each well, the point shows the mean of the values from six simulations. Bars show the total range.

[40] Figure 10 shows ratios of $k_{O,app}/k_O$ and $k_{N,app}/k_N$ compared with median values of Da/Pe . Two sets of rates are shown. One set was estimated from mean particle travel time (Figures 10a and 10b), which is comparable to a field estimate based on physical properties such as velocity and travel distance. A second set of rates were estimated from apparent ages based on simulated SF_6 concentrations (Figures 10c and 10d). In addition to the results from calibrated simulations, shown as points, the calibrated simulations were rerun with ranges of k_O and k_N values to extrapolate the behavior of the simulated systems over ranges of Da/Pe . Also shown are predictions of ratios for simple scenarios of zero time lag, constant source concentrations, and Gaussian dispersion (Figure 10e). The curve for Gaussian dispersion was estimated by assigning values of Da/Pe in equation A9 (Appendix A).

[41] The differences between apparent and true rates depend on the methods used to estimate rates as well as the Da/Pe ratio. As previously shown for CFCs by *Weissmann et al.* [2002], apparent ages derived from simulated SF_6 concentrations in this study were consistently less than the mean particle travel times, owing to the shape of the SF_6 input function and the travel time distributions in simulated well water samples. Accordingly, apparent rates based on apparent ages from simulated SF_6 concentrations were greater than rates based on mean travel times. Travel-time based rates consistently underestimated the true rates (Figures 10a and 10b), while age tracer based rates either underestimated or overestimated the true rate (Figures 10c and 10d). As shown by the continuous curves, increasing Da/Pe (which can result from faster reactions, longer travel times, lower velocities, or greater dispersion) corresponds to larger differences between apparent and true rates. For $k_{N,app}/k_N$, differences were an order of magnitude for some calibrated realizations and were greater than an order of magnitude for uncalibrated scenarios with $Da/Pe > 1$ (Figure 10b).

[42] Comparison of the simulations with simpler scenarios shows that non-Gaussian dispersion and time-varying source concentrations are important factors affecting pre-

diction of apparent rates. Non-Gaussian dispersion (Figure 3) is produced in these simulations by complex geological features such as interconnected high conductivity pathways. In Figure 10a, for $k_{O,app}$ estimated from mean travel time, the $k_{O,app}/k_O$ ratios for simulations are consistently lower (showing stronger effects) than for the analytical solution for Gaussian dispersion. For $k_{N,app}/k_N$, the difference is larger between the analytical solution and simulations due to additional effects of reaction time lag and nonconstant inputs of N. Figure 10e shows the incremental effects of including these different factors in the estimation of $k_{N,app}/k_N$ for realization 1. The most trivial case (and most frequently used for field studies) is the piston flow trend, in which it is assumed there is no mixing and $k_{N,app}/k_N = 1$ for all values of Da/Pe . Scenario I shows the effects of adding Gaussian dispersion with $[O_2]_{cut} = [O_2]_0$, and constant $[NO_3]_0$. Scenario II adds non-Gaussian dispersion. Scenario III adds the calibrated value of $[O_2]_{cut}$ to scenario II to create a time lag, t_{N-lag} , before the onset of denitrification, and scenario IV adds time-varying $[NO_3]_0$ to III. For the calibrated simulation (shown as a point with error bars), the largest changes in $k_{N,app}/k_N$ are produced by adding non-Gaussian dispersion (I to II), and by adding time-varying $[NO_3]_0$ (III to IV). The effects of non-Gaussian dispersion are common to many settings as are the effects of time-varying $[NO_3]_0$ owing to the dramatic increase in applications of chemical N fertilizers starting in the mid-1900s and the persistence of transient historical chemical gradients in aquifers [e.g., *Böhlke*, 2002]. Therefore these influences on estimates of $k_{N,app}$ are likely to be common in field studies of denitrification.

5.4. Factors Affecting Apparent ε

[43] The apparent isotope effects of denitrification (ε_{app}) were most strongly affected by non-Gaussian dispersion and the time lag, t_{N-lag} , before the onset of denitrification (at $[O_2] = [O_2]_{cut}$). Figure 11a shows $\varepsilon_{app}/\varepsilon$ versus Da/Pe for calibrated simulations (points) and $\varepsilon_{app}/\varepsilon$ over ranges of Da/Pe for the same simulations with varying k_N . Values of ε_{app}

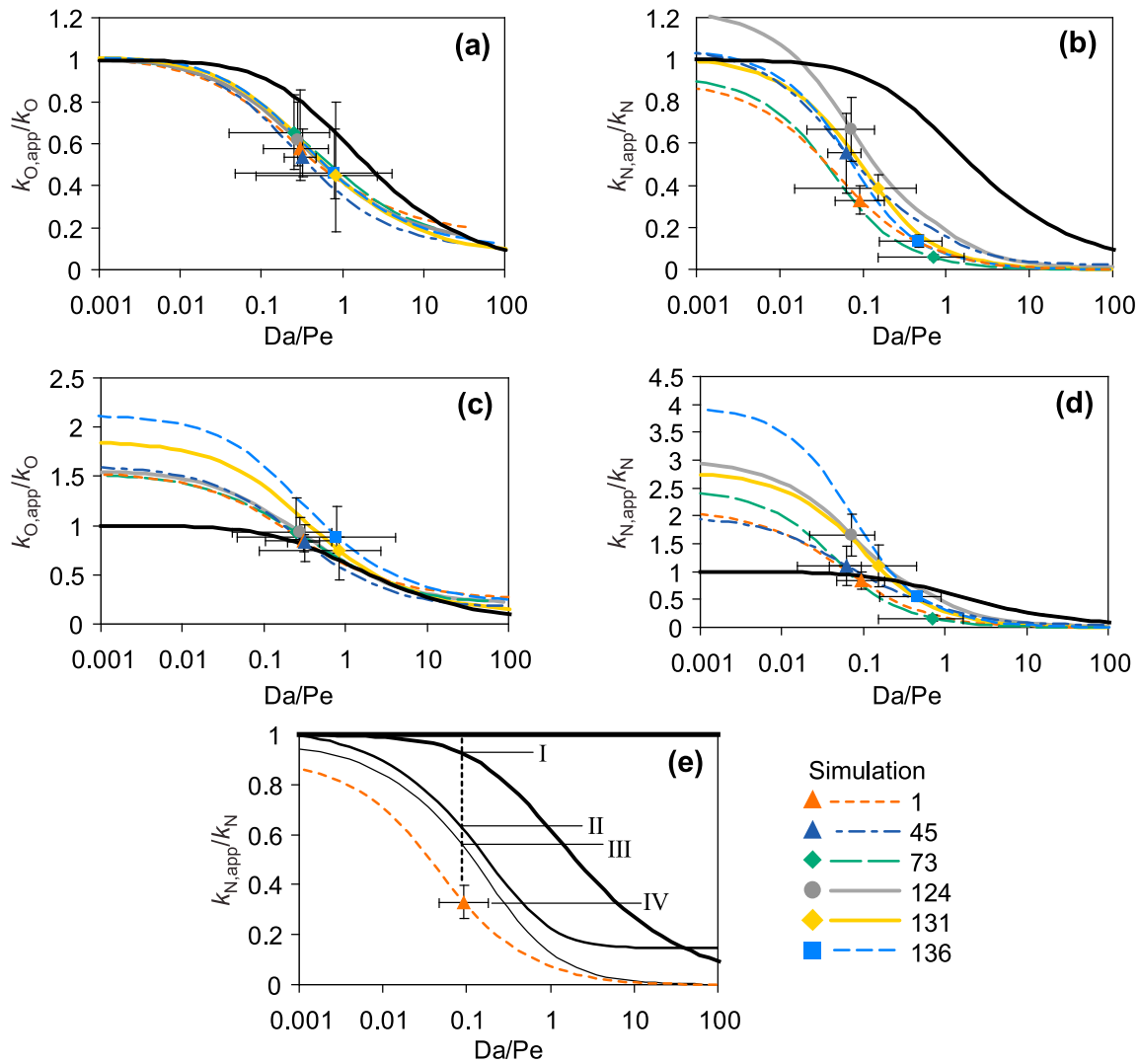


Figure 10. Ratios of apparent to true reaction rate for O_2 reduction (k_{O}) and denitrification (k_{N}) compared with the ratio of the Damköhler (Da) to Peclet (Pe) numbers for (a) $k_{\text{O,app}}$ estimated from mean particle travel time, (b) $k_{\text{N,app}}$ estimated from mean travel time, (c) $k_{\text{O,app}}$ estimated from simulated SF_6 -derived apparent age, (d) $k_{\text{N,app}}$ estimated from simulated SF_6 -derived apparent age, and (e) various scenarios for simulation 1 with $k_{\text{N,app}}$ estimated from mean travel time. For k_{O} and Da/Pe , points are means of values from 14 simulated well samples, and bars show the range. For k_{N} , points are linear least squares best fits to simulated concentrations (Figure 6), and bars show 2 times the standard error. The thick black curves show an analytical solution with constant input and Gaussian dispersion, also shown as scenario I in 9e (see Appendix A). In Figures 10a–10d, curves intersecting points show each simulation with ranges of k_{O} or k_{N} substituted in place of the calibrated value. In Figure 10e, curves show scenarios including the piston flow trend (bold line at $k_{\text{N,app}}/k_{\text{N}} = 1$), scenario I with Gaussian macrodispersion, no time lag and constant input concentrations, scenario II which adds non-Gaussian dispersion to scenario I, scenario III which adds time lag to II, and scenario IV which adds time varying $[\text{NO}_3^-]_0$ to scenario III.

derived from concentrations and isotope ratios in simulated samples are consistently lower than ε and lower than estimates based on the scenario of Gaussian macrodispersion, constant inputs, and zero reaction time lag [Kawanishi *et al.*, 1993] (Figure 11a). Figure 11b shows for simulation 1, the incremental effects of adding various factors which reduce $\varepsilon_{\text{app}}/\varepsilon$ over a range of Da/Pe . Scenarios are the same as for Figure 10e, with the piston flow trend ($\varepsilon_{\text{app}}/\varepsilon = 1$), Gaussian macrodispersion with no time lag and constant input concentrations and stable isotope ratios (scenario I), non-Gaussian dispersion (scenario II), II plus denitrification time

lag (scenario III), and III plus time-varying input $[\text{NO}_3^-]_0$ and $\delta^{15}\text{N}[\text{NO}_3^-]_0$ (scenario IV). For Da/Pe in the range of the calibrated simulation, non-Gaussian dispersion (scenario II) produces twice the effect of Gaussian dispersion (scenario I). The existence of a denitrification time lag (II to III) reduces $\varepsilon_{\text{app}}/\varepsilon$ by an increment which is comparable to that of non-Gaussian dispersion. Figure 11c shows the effects of increasing time lags for each of the realizations at the calibrated value of Da/Pe and with varying input $[\text{NO}_3^-]_0$ and $\delta^{15}\text{N}[\text{NO}_3^-]_0$. Ratios of $\varepsilon_{\text{app}}/\varepsilon$ decrease approximately linearly between time lags of 0 to 30 years. Beyond 30 years,

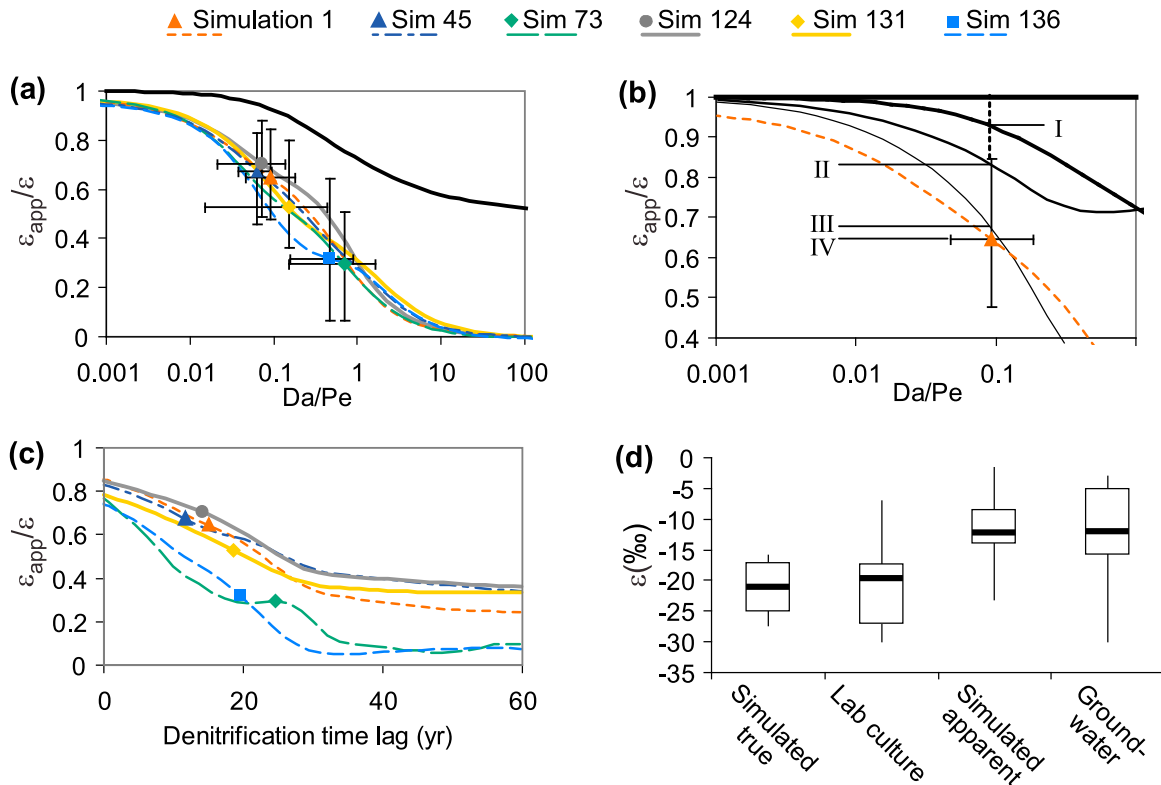


Figure 11. (a) Ratios of apparent to true isotope fractionation parameter (ϵ) for various values of Da/Pe for the six calibrated simulations (points) and for the same simulations with ranges of k_N substituted in place of the calibrated k_N (curves). Points are means of values from 14 simulated well samples, and bars show the range. The thick black curve shows an analytical solution with constant input concentrations, zero time lag, and Gaussian dispersion [Kawanishi *et al.*, 1993]. (b) Simulation 1 with ranges of k_N substituted in place of the calibrated k_N under various scenarios. Scenario numbers (I, II, III, IV) correspond to those in Figure 10. (c) Comparison of ϵ_{app}/ϵ versus time lag for the six scenarios with calibrated $[O_2]_{cut}$ replaced by ranges of $[O_2]_{cut}$ values. Points show the calibrated values. (d) Box plots comparing estimated values of ϵ from a set of heterogeneous simulations (numbers 1, 45, 124, and 136), previous laboratory experiments, piston flow approximations of heterogeneous simulations, and previous field experiments. “Lab culture” values are from Wellman *et al.* [1968], Delwiche and Steyn [1970], Miyake and Wada [1971], Blackmer and Bremner [1977], Wada [1980], Mariotti *et al.* [1981] (omitted 30 degree value), Ollerios [1983], Barford *et al.* [1999], Dhondt *et al.* [2003], and Granger *et al.* [2008]. “Groundwater” values are from Vogel *et al.* [1981], Mariotti *et al.* [1988], Böttcher *et al.* [1990], Fustec *et al.* [1991], Smith *et al.* [1991], McMahon and Böhlke [1996], Koba *et al.* [1997], Aravena and Robertson [1998], Mengis *et al.* [1999], Fryar *et al.* [2000], Böhlke *et al.* [2002], Griggs *et al.* [2003], Fukuhara *et al.* [2007], Singleton *et al.* [2007] (excluding values derived using three or fewer samples), Green *et al.* [2008a], and Hatzinger *et al.* [2009].

ratios of ϵ_{app}/ϵ are relatively constant. The break in slope coincides approximately with the historical increase in $[NO_3^-]_0$ (Figure 4a) which is also reflected as a sharp break in slope in the calibrated distributions of N mass with respect to travel time in individual samples (Figure 3).

[44] These results provide a basis for comparing ϵ_{app} estimates in different mixing environments and show that the effect of dispersion on apparent fractionation parameters can account for differences between ϵ values observed in laboratory batch experiments versus field studies. Field studies commonly have neglected mixing, and provided estimates that are analogous to the ϵ_{app} values in these numerical experiments. Among previously reported estimates from aquifers, the interquartile range of ϵ_{app} is from -5 to -16‰ (Figure 11d). Laboratory incubations typically are relatively unaffected by dispersive mixing and produce estimates of ϵ

that are comparable to the true ϵ values assigned in these numerical experiments. The interquartile range of previously reported laboratory estimates is -17 to -27‰ . To test the possibility that the difference between laboratory and field estimates of ϵ result from dispersive mixing, calibrated simulations 1, 45, 124, and 136 were selected as representative of laboratory results, based on the criteria of having ϵ values close to, or in the range of, the laboratory interquartiles (“simulated true” on Figure 11d). For these simulations, the range, interquartiles, and medians were calculated for the set of all wells in all simulations (“simulated apparent” on Figure 11d). These results resemble the literature values for ϵ_{app} from groundwater, indicating that dispersive mixing is a possible explanation for the observed difference between laboratory and groundwater estimates of ϵ .

[45] As ε values are increasingly used to study the rates and extents of natural attenuation of NO_3^- and other contaminants [e.g., *Meckenstock et al.*, 2004; *Abe and Hunkeler*, 2006; *Blum et al.*, 2009], effects of physical heterogeneity are likely to influence predictions of contaminant fate and transport. For the calibrated scenarios, an apparent denitrification ε value of -10‰ based on sample analyses is consistent with true in situ denitrification ε ranging from -14‰ to -34‰ . For a prediction of f_N from changes in $\delta^{15}\text{N}[\text{NO}_3^-]$, this range of ε results in a factor of 2 difference between the high and low estimates of f_N . Much larger differences can be expected for higher Da/Pe ratios due, for example, to faster reactions or longer travel times (Figures 10 and 11). It is emphasized that these results were obtained in model aquifer systems with uniform reaction rates, whereas additional biases could be present where reaction rates differ between geological units. In some situations, apparent isotope effects may be almost nonexistent, as at boundaries of two zones, one of which is reactive and the other of which is not. Situations like these include sediment-water interfaces and wells or flow paths that include abrupt redox transitions in aquifers [e.g., *McMahon et al.*, 1999; *Lehmann et al.*, 2003; *Böhlke et al.*, 2007].

6. Conclusions

[46] In a sedimentary aquifer in the San Joaquin Valley, California, field measurements and numerical experiments demonstrate that physical heterogeneity results in substantial mixing of waters with a range of travel times in individual samples from short-screened monitoring wells. The blending of concentrations of anthropogenic atmospheric tracers, O_2 , NO_3^- , and N_2 over the distribution of travel times reduces the magnitudes of apparent groundwater ages, reaction kinetic coefficients, k , and isotopic fractionation parameters, ε , that are estimated from sample concentrations. For calibrated model scenarios from the San Joaquin study site, estimates of apparent denitrification rate and ε in individual wells were lower than true values by factors as high as 10. For faster reactions and stronger dispersion the effect increases such that at ratios of Da/Pe greater than 10, simulated apparent reaction rates and ε values are orders of magnitude lower than the true values. These results contrast with previous studies indicating smaller differences between true and apparent parameters in relatively simple scenarios. In this study, the more pronounced effects result from combined influence of non-Gaussian dispersion produced by macroscopic geological heterogeneity, time lag before the onset of denitrification due to inhibition by O_2 , and time-varying input concentrations of NO_3^- due to increases in agricultural applications over time. Because many aquifer systems include geological heterogeneity, redox zonation, and nonuniform input histories, it can be generalized that the effects of mixing on apparent reaction kinetic coefficients and fractionation parameters for reactive transport of NO_3^- will be important across a wide range of sites.

[47] For reaction and fractionation parameters, differences between field and laboratory estimates may result from the effects of dispersive mixing in aquifers. Field estimates of ε in groundwater have tended to be smaller in magnitude than laboratory estimates. Simulations assigning true values of ε corresponding to homogeneous laboratory experiments

yield apparent values of ε that are similar to those from previous field studies. For the oxygen threshold inhibiting denitrification, $[\text{O}_2]_{\text{cut}}$, simulations show that apparent values are systematically greater than true values, which is consistent with previous observations in laboratory and field studies. The influence of mixing and dispersion should be considered whenever parameter values are compared among different settings or across different transport scales in a single setting. Additional work remains to elucidate the effects of apparent versus true rates and fractionation parameters on forecasts of water quality, and to address more complicated scenarios with spatially variable reaction rates, alternative reaction models, and transient flow conditions. These developments will allow more robust cross-site comparisons of rates and fractionation parameters, and they should improve the reliability of contaminant transport models that are calibrated using chemical and isotopic data.

Appendix A

[48] For a 1-D homogeneous, semi-infinite system with constant first-order reaction and dispersion beyond a constant flux boundary, and constant resident concentration at the downgradient boundary [*Kawanishi et al.*, 1993], the apparent decay coefficient is a function of the ratio of the Peclet and Damköhler numbers, as shown below.

[49] The apparent decay coefficient is defined using the first-order decay equation,

$$k_{i,\text{app}} = \frac{-\ln\left(\frac{\bar{S}_i(x)}{\bar{S}_i(x=0)}\right)}{t}, \quad (\text{A1})$$

where $k_{i,\text{app}}$ is the apparent decay coefficient for constituent i , \bar{S}_i is the dimensionless resident concentration of solute i at some distance, x , beyond the point at which the reaction begins. \bar{S}_i is defined by

$$\bar{S}_i = S/S_m, \quad (\text{A2})$$

where S is the resident concentration and S_m is the flux concentration at $x = 0$. The dimensionless concentration is [*Kawanishi et al.*, 1993]

$$\bar{S}_i(x) = \frac{2}{1+p} \exp\left(\frac{(1-p)PeX}{2}\right), \quad (\text{A3})$$

where X is the dimensionless distance, x/L , and L is the distance to the downgradient boundary. The Peclet number is here defined by

$$Pe = \frac{Lv}{D}. \quad (\text{A4})$$

[50] The variable p is defined by

$$p = (1 + 4\Gamma)^{\frac{1}{2}}, \quad (\text{A5})$$

where

$$\Gamma = \frac{kD}{v^2} = \frac{Da}{Pe}. \quad (\text{A6})$$

Da is a Damköhler number,

$$Da = \frac{kL}{v}. \quad (A7)$$

[51] Dividing both sides of equation (A1) by k_i and substitution of equation (A3) for $\bar{S}_i(x)$ and $\bar{S}_i(x=0)$ gives

$$\frac{k_{i,app}}{k_i} = \frac{-\ln\left(\exp\left(\frac{(1-p)PeX}{2}\right)\right)}{k_i t}, \quad (A8)$$

which simplifies to

$$\frac{k_{i,app}}{k_i} = \frac{-\left(1 - (1 + 4\Gamma)^{-\frac{1}{2}}\right)}{2\Gamma}. \quad (A9)$$

[52] **Acknowledgments.** Peter Dileanis, Joe Domagalski, Charlie Kratzer, Patricia Orlando, Celia Zamora, and others completed the field work described in this study. Karen Burow provided well log data to assist with geostatistical realizations. Claire Tiedeman and Matt Tonkin provided guidance for numerical calibrations. Eric LaBolle assisted with use of RWHet. Hedef Essaid and Megan Young provided helpful suggestions for the manuscript. This study was conducted as part of the USGS National Water Quality Assessment Program and National Research Program.

References

- Abe, Y., and D. Hunkeler (2006), Does the Rayleigh equation apply to evaluate field isotope data in contaminant hydrogeology?, *Environ. Sci. Technol.*, 40(5), 1588–1596, doi:10.1021/es051128p.
- Aravena, R., and W. D. Robertson (1998), Use of multiple isotope tracers to evaluate denitrification in ground water: Study of nitrate from a large-flux septic system plume, *Ground Water*, 36(6), 975–982, doi:10.1111/j.1745-6584.1998.tb02104.x.
- Barford, C. C., J. P. Montoya, M. A. Altabet, and R. Mitchell (1999), Steady-state nitrogen isotope effects of N_2 and N_2O production in Paracoccus denitrificans, *Appl. Environ. Microbiol.*, 65(3), 989–994.
- Blackmer, A. M., and J. M. Bremner (1977), Nitrogen isotope discrimination in denitrification of nitrate in soils, *Soil Biol. Biochem.*, 9(2), 73–77, doi:10.1016/0038-0717(77)90040-2.
- Blum, P., D. Hunkeler, M. Weede, C. Beyer, P. Grathwohl, and B. Morasch (2009), Quantification of biodegradation for o-xylene and naphthalene using first order decay models, Michaelis-Menten kinetics and stable carbon isotopes, *J. Contam. Hydrol.*, 105(3–4), 118–130, doi:10.1016/j.jconhyd.2008.11.009.
- Böhlke, J. K. (2002), Groundwater recharge and agricultural contamination, *Hydrogeol. J.*, 10(1), 153–179, doi:10.1007/s10040-001-0183-3. (Erratum, *Hydrogeol. J.*, 10(3), 438–439, doi:10.1007/s10040-002-0210-z.)
- Böhlke, J. K., R. Wanty, M. Tuttle, G. Delin, and M. Landon (2002), Denitrification in the recharge area and discharge area of a transient agricultural nitrate plume in a glacial outwash sand aquifer, Minnesota, *Water Resour. Res.*, 38(7), 1105, doi:10.1029/2001WR000663.
- Böhlke, J. K., M. E. O'Connell, and K. L. Prestegard (2007), Ground water stratification and delivery of nitrate to an incised stream under varying flow conditions, *J. Environ. Qual.*, 36(3), 664–680, doi:10.2134/jeq2006.0084.
- Böttcher, J., O. Strebel, S. Voerkelius, and H. L. Schmidt (1990), Using isotope fractionation of nitrate-nitrogen and nitrate-oxygen for evaluation of microbial denitrification in a sandy aquifer, *J. Hydrol.*, 114(3), 413–424, doi:10.1016/0022-1694(90)90068-9.
- Busenberg, E., and L. N. Plummer (1992), Use of chlorofluorocarbons (CCl_3F and CCl_2F_2) as hydrologic tracers and age-dating tools: The alluvium and terrace system of central Oklahoma, *Water Resour. Res.*, 28(9), 2257–2283, doi:10.1029/92WR01263.
- Busenberg, E., and L. N. Plummer (2000), Dating young groundwater with sulfur hexafluoride: Natural and anthropogenic sources of sulfur hexafluoride, *Water Resour. Res.*, 36(10), 3011–3030, doi:10.1029/2000WR900151.
- Capel, P. D., K. A. McCarthy, and J. E. Barbash (2008), National, holistic, watershed-scale approach to understand the sources, transport, and fate of agricultural chemicals, *J. Environ. Qual.*, 37(3), 983–983, doi:10.2134/jeq2007.0226.
- Carle, S. F., and G. E. Fogg (1996), Transition probability-based indicator geostatistics, *Math. Geol.*, 28(4), 453–476, doi:10.1007/BF02083656.
- Carle, S. F., and G. E. Fogg (1997), Modeling spatial variability with one and multidimensional continuous-lag Markov chains, *Math. Geol.*, 29(7), 891–918, doi:10.1023/A:1022303706942.
- Chen, F., Q. Xia, and L. K. Ju (2003), Aerobic denitrification of *Pseudomonas aeruginosa* monitored by online NAD (P) H fluorescence, *Appl. Environ. Microbiol.*, 69(11), 6715–6722, doi:10.1128/AEM.69.11.6715-6722.2003.
- Clark, S. K., and T. M. Johnson (2008), Effective isotopic fractionation factors for solute removal by reactive sediments: A laboratory microcosm and slurry study, *Environ. Sci. Technol.*, 42(21), 7850–7855, doi:10.1021/es801814v.
- Conrad, R. (1996), Soil microorganisms as controllers of atmospheric trace gases (H_2 , CO, CH_4 , OCS, N_2O , and NO), *Microbiol. Rev.*, 60(4), 609–640.
- Cook, P. G., and J. K. Böhlke (2000), Determining timescales for groundwater flow and solute transport, in *Environmental Tracers in Subsurface Hydrology*, edited by P. Cook and A. L. Herczeg, pp. 1–30, Kluwer Acad., Boston, Mass.
- Coyne, M. S. (2008), Biological denitrification, in *Nitrogen in Agricultural Systems*, *Aeron. Monogr.*, vol. 49, edited by J. S. Schepers and W. Raun, pp. 201–253, Am. Soc. of Agron./Crop Sci. Soc. of Am./Soil. Sci. Soc. of Am., Madison, Wis.
- Delwiche, C. C., and P. L. Steyn (1970), Nitrogen isotope fractionation in soils and microbial reactions, *Environ. Sci. Technol.*, 4(11), 929–935, doi:10.1021/es60046a004.
- Dhondt, K., P. Boeckx, O. Van Cleemput, and G. Hofman (2003), Quantifying nitrate retention processes in a riparian buffer zone using the natural abundance of N-15 in NO_3 , *Rapid Commun. Mass Spectrom.*, 17(23), 2597–2604, doi:10.1002/rcm.1226.
- Doherty, J. (2008), *PEST: Model-Independent Parameter Estimation User Manual*, 5th ed., 336 pp., Watermark Comput., Corinda, Queensl., Australia.
- Domagalski, J. L., S. P. Phillips, E. R. Bayless, C. Zamora, C. Kendall, R. A. Wildman, and J. G. Hering (2008), Influences of the unsaturated, saturated, and riparian zones on the transport of nitrate near the Merced River, California, USA, *Hydrogeol. J.*, 16(4), 675–690, doi:10.1007/s10040-007-0266-x.
- Fryar, A. E., S. A. Macko, W. F. Mullican, K. D. Romanak, and P. C. Bennett (2000), Nitrate reduction during ground-water recharge, southern High Plains, Texas, *J. Contam. Hydrol.*, 40(4), 335–363, doi:10.1016/S0169-7722(99)00059-5.
- Fukuhara, H., F. Nemoto, Y. Takeuchi, and N. Toda (2007), Nitrate dynamics in a reed belt of a shallow sand dune lake in Japan: Analysis of nitrate retention using stable nitrogen isotope ratios, *Hydrobiologia*, 584(1), 49–58, doi:10.1007/s10750-007-0589-6.
- Fustec, E., A. Mariotti, X. Grillo, and J. Sajus (1991), Nitrate removal by denitrification in alluvial ground-water—Role of a former channel, *J. Hydrol.*, 123(3–4), 337–354, doi:10.1016/0022-1694(91)90098-3.
- Gelhar, L. W. (1986), Stochastic subsurface hydrology from theory to applications, *Water Resour. Res.*, 22(9), S135–S145, doi:10.1029/WR022i09Sp0135S.
- Granger, J., D. M. Sigman, M. F. Lehmann, and P. D. Tortell (2008), Nitrogen and oxygen isotope fractionation during dissimilatory nitrate reduction by denitrifying bacteria, *Limnol. Oceanogr.*, 53(6), 2533–2545.
- Green, C. T., L. J. Puckett, J. K. Böhlke, B. A. Bekins, S. P. Phillips, L. J. Kauffman, J. M. Denver, and H. M. Johnson (2008a), Limited occurrence of denitrification in four shallow aquifers in agricultural areas of the United States, *J. Environ. Qual.*, 37(3), 994–1009, doi:10.2134/jeq2006.0419.
- Green, C. T., L. H. Fisher, and B. A. Bekins (2008b), Nitrogen fluxes through unsaturated zones in five agricultural settings across the United States, *J. Environ. Qual.*, 37(3), 1073–1085, doi:10.2134/jeq2007.0010.
- Griggs, E. M., L. R. Kump, and J. K. Böhlke (2003), The fate of wastewater-derived nitrate in the subsurface of the Florida Keys: Key Colony Beach, Florida, *Estuarine Coastal Shelf Sci.*, 58(3), 517–539, doi:10.1016/S0272-7714(03)00131-8.
- Groffman, P. M., M. A. Altabet, J. K. Böhlke, K. Butterbach-Bahl, M. B. David, M. K. Firestone, A. E. Giblin, T. M. Kana, L. P. Nielsen, and M. A. Voytek (2006), Methods for measuring denitrification:

- Diverse approaches to a difficult problem, *Ecol. Appl.*, 16(6), 2091–2122, doi:10.1890/1051-0761(2006)016[2091:MFMDDA]2.0.CO;2.
- Harbaugh, A. W., E. R. Banta, M. C. Hill, and M. G. McDonald (2000), MODFLOW-2000, the U. S. Geological Survey modular ground-water model—User guide to modularization concepts and the ground-water flow process, *U.S. Geol. Surv. Open File Rep.* 92, 134 pp.
- Hatzinger, P. B., J. K. Böhlke, N. C. Sturchio, B. Gu, L. J. Heraty, and R. C. Borden (2009), Fractionation of stable isotopes in perchlorate and nitrate during in situ biodegradation in a sandy aquifer, *Environ. Chem.*, 6(1), 44–52, doi:10.1071/EN09008.
- Heaton, T. H. E., and J. C. Vogel (1981), Excess air in groundwater, *J. Hydrol.*, 50(1–3), 201–216, doi:10.1016/0022-1694(81)90070-6.
- Kawanishi, T., Y. Hayashi, N. Kihou, T. Yoneyama, and Y. Ozaki (1993), Dispersion effect on the apparent nitrogen isotope fractionation factor associated with denitrification in soil; evaluation by a mathematical model, *Soil Biol. Biochem.*, 25(3), 349–354, doi:10.1016/0038-0717(93)90134-W.
- Koba, K., N. Tokuchi, E. Wada, T. Nakajima, and G. Iwatsubo (1997), Intermittent denitrification: The application of a N-15 natural abundance method to a forested ecosystem, *Geochim. Cosmochim. Acta*, 61(23), 5043–5050, doi:10.1016/S0016-7037(97)00284-6.
- LaBolle, E. M., J. Quastel, G. E. Fogg, and J. Gravner (2000), Diffusion processes in composite porous media and their numerical integration by random walks: Generalized stochastic differential equations with discontinuous coefficients, *Water Resour. Res.*, 36(3), 651–662, doi:10.1029/1999WR900224.
- Lehmann, M. F., P. Reichert, S. M. Bernasconi, A. Barbieri, and J. A. McKenzie (2003), Modelling nitrogen and oxygen isotope fractionation during denitrification in a lacustrine redox-transition zone, *Geochim. Cosmochim. Acta*, 67(14), 2529–2542, doi:10.1016/S0016-7037(03)00085-1.
- Lesser, L. E., P. C. Johnson, R. Aravena, G. E. Spinnler, C. L. Bruce, and J. P. Salanitro (2008), An evaluation of compound-specific isotope analyses for assessing the biodegradation of MTBE at Port Hueneme, CA, *Environ. Sci. Technol.*, 42(17), 6637–6643, doi:10.1021/es703029s.
- Marchand, D. E., and A. Allwardt (1978), Preliminary geologic map showing quaternary deposits of the northeastern San Joaquin Valley, U.S. Geol. Surv. Misc. Field Stud. Map, MF-945.
- Marchand, D. E., and A. Allwardt (1981), Late Cenozoic stratigraphic units, northeastern San Joaquin Valley, California, *U.S. Geol. Surv. Bull.*, 1470, 70 pp.
- Mariotti, A., J. C. Germon, P. Hubert, P. Kaiser, R. Letolle, A. Tardieux, and P. Tardieux (1981), Experimental determination of nitrogen kinetic isotope fractionation: Some principles; illustration for the denitrification and nitrification processes, *Plant Soil*, 62(3), 413–430, doi:10.1007/BF02374138.
- Mariotti, A., A. Landreau, and B. Simon (1988), ¹⁵N isotope biogeochemistry and natural denitrification process in groundwater: Application to the chalk aquifer of northern France, *Geochim. Cosmochim. Acta*, 52(7), 1869–1878, doi:10.1016/0016-7037(88)90010-5.
- McMahon, P. B., and J. K. Böhlke (1996), Denitrification and mixing in a stream/aquifer system: Effects on nitrate loading to surface water, *J. Hydrol.*, 186(1–4), 105–128, doi:10.1016/S0022-1694(96)03037-5.
- McMahon, P. B., and J. K. Böhlke (2006), Regional patterns in the isotopic composition of natural and anthropogenic nitrate in groundwater, High Plains, USA, *Environ. Sci. Technol.*, 40(9), 2965–2970, doi:10.1021/es052229q.
- McMahon, P. B., J. K. Böhlke, and B. W. Bruce (1999), Denitrification in marine shales in northeastern Colorado, *Water Resour. Res.*, 35(5), 1629–1642, doi:10.1029/1999WR900004.
- McMahon, P. B., J. K. Böhlke, and S. C. Christenson (2004), Geochemistry, radiocarbon ages, and paleorecharge conditions along a transect in the central High Plains aquifer, southwestern Kansas, USA, *Appl. Geochem.*, 19(11), 1655–1686, doi:10.1016/j.apgeochem.2004.05.003.
- McMahon, P. B., J. K. Böhlke, L. J. Kauffman, K. L. Kipp, M. K. Landon, C. A. Crandall, K. R. Burrow, and C. J. Brown (2008), Source and transport controls on the movement of nitrate to public supply wells in selected principal aquifers of the United States, *Water Resour. Res.*, 44, W04401, doi:10.1029/2007WR006252.
- Meckenstock, R. U., B. Morasch, C. Griebler, and H. H. Richnow (2004), Stable isotope fractionation analysis as a tool to monitor biodegradation in contaminated aquifers, *J. Contam. Hydrol.*, 75(3–4), 215–255, doi:10.1016/j.jconhyd.2004.06.003.
- Mengis, M., S. L. Schiff, M. Harris, M. C. English, R. Aravena, R. J. Elgood, and A. MacLean (1999), Multiple geochemical and isotopic approaches for assessing ground water NO₃⁻ elimination in a riparian zone, *Ground Water*, 37(3), 448–457, doi:10.1111/j.1745-6584.1999.tb01124.x.
- Miyake, Y., and E. Wada (1971), The isotope effect on the nitrogen in biochemical oxidation-reduction reactions, *Rec. Oceanogr. Works Jpn.*, 11, 1–6.
- Nakamura, K., T. Harter, Y. Hirono, H. Horino, and T. Mitsuno (2004), Assessment of root zone nitrogen leaching as affected by irrigation and nutrient management practices, *Vadose Zone J.*, 3(4), 1353–1366, doi:10.2113/3.4.1353.
- National Research Council (2000), *Natural Attenuation for Groundwater Remediation*, 292 pp., Natl. Acad. of Sci., Washington, D. C.
- Nolan, B. T., L. J. Puckett, L. Ma, C. T. Green, E. R. Bayless, and R. W. Malone (2010), Predicting unsaturated zone nitrogen mass balances in agricultural settings of the United States, *J. Environ. Qual.*, 39, 1051–1065, doi:10.2134/jeq2009.0310.
- Olleros, T. (1983), Kinetische isotopeffekte der arginase- und nitratreduktase-reaktion: Ein beitrag zur aufklärung der entsprechenden reaktionsmechanismen, Ph.D. dissertation, Tech. Univ. München, Weihenstephan, Germany.
- Phillips, S. P., C. T. Green, K. R. Burrow, J. L. Shelton, and D. L. Lewis (2007), Simulation of multiscale ground-water flow in part of the north-eastern San Joaquin Valley, California, *U.S. Geol. Surv. Sci. Invest. Rep.*, 2007-5009.
- Pollock, D. W. (1994), User's guide for MODPATH/MODPATH-PLOT, version 3: A particle tracking post-processing package for MODFLOW, the U.S. Geological Survey finite-difference ground-water flow model, *U.S. Geol. Surv. Open File Rep.*, 94-464.
- Revesz, K., J. K. Böhlke, R. L. Smith, and T. Yoshinari (1999), Stable isotope composition of dissolved O₂ undergoing respiration in a ground-water contamination gradient, *U.S. Geol. Surv. Water Resour. Invest. Rep.*, 99-4018C.
- Seitzinger, S., J. A. Harrison, J. K. Böhlke, A. F. Bouwman, R. Lowrance, B. Peterson, C. Tobias, and G. V. Drecht (2006), Denitrification across landscapes and waterscapes: A synthesis, *Ecol. Appl.*, 16(6), 2064–2090, doi:10.1890/1051-0761(2006)016[2064:DALAWA]2.0.CO;2.
- Sigman, D. M., K. L. Casciotti, M. Andreani, C. Barford, M. Galanter, and J. K. Böhlke (2001), A bacterial method for the nitrogen isotopic analysis of nitrate in seawater and freshwater, *Anal. Chem.*, 73(17), 4145–4153, doi:10.1021/ac010088e.
- Singleton, M. J., B. K. Esser, J. E. Moran, G. B. Hudson, W. W. McNab, and T. Harter (2007), Saturated zone denitrification: Potential for natural attenuation of nitrate contamination in shallow groundwater under dairy operations, *Environ. Sci. Technol.*, 41(3), 759–765, doi:10.1021/es061253g.
- Smith, R. L., B. L. Howes, and J. H. Duff (1991), Denitrification in nitrate-contaminated groundwater—Occurrence in steep vertical geochemical gradients, *Geochim. Cosmochim. Acta*, 55(7), 1815–1825, doi:10.1016/0016-7037(91)90026-2.
- Smith, R. L., J. K. Böhlke, S. P. Garabedian, K. M. Revesz, and T. Yoshinari (2004), Assessing denitrification in groundwater using natural gradient tracer tests with ¹⁵N: In situ measurement of a sequential multistep reaction, *Water Resour. Res.*, 40, W07101, doi:10.1029/2003WR002919.
- Tiedje, J. M. (1988), Ecology of denitrification and dissimilatory nitrate reduction to ammonium, in *Biology of Anaerobic Microorganisms*, edited by A. J. B. Zehnder, pp. 179–244, Wiley-Intersci., New York.
- Tompson, A. F. B., S. F. Carle, N. D. Rosenberg, and R. M. Maxwell (1999), Analysis of groundwater migration from artificial recharge in a large urban aquifer: A simulation perspective, *Water Resour. Res.*, 35(10), 2981–2998, doi:10.1029/1999WR900175.
- Varni, M., and J. Carrera (1998), Simulation of groundwater age distributions, *Water Resour. Res.*, 34(12), 3271–3281, doi:10.1029/98WR02536.
- Vogel, J. C., A. S. Talma, and T. H. E. Heaton (1981), Gaseous nitrogen as evidence for denitrification in groundwater, *J. Hydrol.*, 50(1–3), 191–200, doi:10.1016/0022-1694(81)90069-X.
- Wada, E. (1980), Nitrogen isotope fractionation and its significance in biogeochemical processes occurring in marine environments, in *Isotope Marine Chemistry*, edited by E. D. Goldberg and Y. Horibe, pp. 375–398, Uchida Rokakuho, Tokyo.
- Weissmann, G. S., Y. Zhang, E. M. LaBolle, and G. E. Fogg (2002), Dispersion of groundwater age in an alluvial aquifer system, *Water Resour. Res.*, 38(10), 1198, doi:10.1029/2001WR000907.
- Wellman, R. P., F. D. Cook, and H. R. Krouse (1968), Nitrogen-15—Microbiological alteration of abundance, *Science*, 161(3838), 269–270, doi:10.1126/science.161.3838.269.

- Woolfenden, L., and T. R. Ginn (2009), Modeled ground water age distributions, *Ground Water*, 47(4), 547–557, doi:10.1111/j.1745-6584.2008.00550.x.
- Zuber, A. (1986), Mathematical models for the interpretation of environmental radioisotopes in groundwater systems, in *Handbook of Environmental Isotope Geochemistry, Part B*, edited by P. Fritz and J. C. Fontes, pp. 1–60, Elsevier, Amsterdam.
- Zumft, W. G. (1997), Cell biology and molecular basis of denitrification, *Microbiol. Mol. Biol. Rev.*, 61(4), 533–616.
-
- B. A. Bekins and C. T. Green, U.S. Geological Survey, 345 Middlefield Rd., Menlo Park, CA 94025, USA. (ctgreen@usgs.gov)
- J. K. Böhlke, U.S. Geological Survey, 12201 Sunrise Valley Dr., Reston, VA 20192, USA.
- S. P. Phillips, U.S. Geological Survey, 6000 J St., Placer Hall, Sacramento, CA 95819, USA.